Surface-averaged quantities in turbulent reacting flows and relevant evolution equations

Rixin Yu
Division of Fluid Mechanics, Department of Energy Sciences, Lund University, 22100 Lund, Sweden

Andrei N. Lipatnikov
Department of Mechanics and Maritime Sciences, Chalmers University of Technology, Göteborg 412 96, Sweden

(Received 19 March 2019; revised manuscript received 2 June 2019; published 16 July 2019)

While quantities conditioned to an isosurface of reaction progress variable c, which characterizes fluid state in a turbulent reacting flow, have been attracting rapidly growing interest in the recent literature, a mathematical and physical framework required for research into such quantities has not yet been elaborated properly. This paper aims at filling two fundamental gaps in this area, i.e., (i) ambiguities associated with a definition of a surface-averaged quantity and (ii) the lack of rigorous equations that describe evolutions of such quantities. In the first (theoretical) part of the paper, (a) analytical relations between differently defined (area-weighted and unweighted) surface-averaged quantities are obtained and differences between them (quantities) are discussed, (b) a unified method for deriving an evolution equation for bulk area-weighted surface-averaged value of a local characteristic ϕ of a turbulent reacting flow is developed, and (c) the method is applied for deriving evolution equations for the bulk area-weighted surface-averaged reaction-surface density $|\nabla c|$, local reaction-wave thickness $1/|\nabla c|$, and local displacement speed S_d, i.e., the speed of an isosurface of the $c(\boldsymbol{x}, t)$ field with respect to the local flow. In the second (numerical) part of the paper, direct numerical simulation data obtained recently from a highly turbulent reaction wave are analyzed in order to (1) highlight substantial differences between area-weighted and unweighted surface-averaged quantities and (2) show that various terms in the derived evolution equations are amenable to accurate numerical evaluation in spite of appearance of the so-called zero-gradient points [C. H. Gibson, Phys. Fluids **11**, 2305 (1968)] in a highly turbulent medium. Finally, the obtained analytical and numerical results are used to shed light on the paradox of local flame thinning and broadening which is widely discussed in the turbulent combustion literature.

DOI: 10.1103/PhysRevE.100.013107

I. INTRODUCTION

A problem of the influence of turbulence on reaction waves is straightforwardly relevant to various phenomena ranging from reactions in aqueous solution [1], combustion [2–6], and deflagration-to-detonation transition [7,8] under terrestrial conditions to evolution of thermonuclear type Ia supernovae [9,10] in the Universe. This nonlinear and multiscale problem attracted much attention since the 1940's when significant acceleration of flame propagation by turbulence was found. Following pioneering work by Damköhler [11] and Shelkin [12], the effect is commonly attributed to an increase in the flame-surface area due to wrinkles of the surface, caused by turbulent eddies. While such a simple explanation was applied to weakly and moderately turbulent reacting flows over decades, recent direct numerical simulation (DNS) data [13–15] have indicated that the flame-surface-area increase controls burning rate even if the root mean square (rms) turbulent velocity u' is much (by a factor of 10 or even 100) larger than the laminar flame speed S_L.

Generation of flame surface area by turbulence is commonly characterized using either (i) flame-surface density (FSD) $|\nabla c|$, whose mean value yields mean flame-surface area within an infinitesimal volume dV [16], or (ii) the local stretch rate, which is defined as follows:

$$\mathcal{K} \equiv a_t - S_d\kappa = \nabla \cdot \boldsymbol{u} - a_n + S_d\kappa \qquad (1)$$

and is well known [17–20] to directly quantify the rate of change of the area δA of an infinitesimal element of a self-propagating surface, i.e., $d(\delta A)/dt = \mathcal{K}\delta A$. Here, c is a combustion progress variable, which (i) can be defined by properly normalizing temperature, density, or mass fraction of a major species and (ii) is commonly used to characterize the state of a reacting mixture (typically, $c = 0$ and 1 in fresh reactants and equilibrium products, respectively); $a_n \equiv n_i n_j \partial u_i/\partial x_j$ and $a_t = \nabla \cdot \boldsymbol{u} - a_n$ are the normal and tangential strain rates, respectively; $\boldsymbol{u}$ is the local velocity vector; $\kappa = -\nabla \cdot \boldsymbol{n}$ is the local flame curvature; the unit vector $\boldsymbol{n} = \nabla c/|\nabla c|$ is normal to the local flame surface and points to the products; and S_d, which will be defined later, is the local displacement speed, i.e., the speed of the considered flame surface with respect to the local flow.

In spite of the paramount importance of the increase in the flame-surface area, the influence of turbulence on premixed combustion is not solely reduced to this physical mechanism. In particular, turbulent eddies can significantly change the local flame structure, thickness, and, hence, the local heat-release rate, with these phenomena being of paramount importance in lean mixtures of light fuels (hydrogen or syngas) with the air [21–27]. Such effects are also often characterized using $|\nabla c|$ and $\mathcal{K}$. The former quantity directly yields the inverse of the local flame thickness and, according to the theory of laminar premixed flames subject to large-scale perturbations

[17,28], difference between the local flame speed or burning rate and its unperturbed value is controlled by the local stretch rate.

For the above reasons, investigation of the behavior of FSD $|\nabla c|$, its inverse value $1/|\nabla c|$, stretch rate $\mathcal{K}$, and its components is of paramount importance for understanding the influence of turbulence on premixed flames or another reaction wave. Accordingly, the aforementioned local quantities $\phi = \{|\nabla c|,\ 1/|\nabla c|,\ \mathcal{K},\ a_t,\ a_n,\ S_d,\ \kappa,\ S_d\kappa\}$ were in the focus of DNS research into turbulent constant-density, single-reaction waves [15,20,29], turbulent single-step-chemistry flames [30–39], or turbulent complex-chemistry flames [40–43]. In such papers, either statistics of $\phi(\boldsymbol{x}, t)$ conditioned to an isosurface of $c(\boldsymbol{x}, t) = \hat{c}$ are analyzed or different mean or filtered terms in a transport equation for $\phi(\boldsymbol{x}, t)$ are extracted from DNS data and compared.

However, results obtained using these two methods (conditioned statistics and mean transport equations) cannot directly be compared because transport equations for mean quantities are well known to be different from transport equations for the counterpart conditioned quantities [21]. For instance, divergence of velocity conditioned to a particular mixture state does not vanish in constant-density turbulent flows [44]. Therefore, there is need for deriving transport equations for quantities conditioned to isosurfaces and extracted from various DNS databases. This work aims at making a first step to fill this gap by (i) developing a unified method for deriving an evolution equation for the bulk (i.e., averaged over the entire flame volume) value of the surface-averaged quantity ϕ and (ii) applying the method to $\phi = |\nabla c|$, $1/|\nabla c|$, and S_d.

While the use of such bulk quantities results in missing information about evolution of the surface-averaged quantities along the normal to the mean flame brush, various surface-conditioned quantities integrated along the normal were widely studied to explore flame-turbulence interaction in the recent literature [35,38,42,43,45–47]. Thus, research into such quantities has its own fundamental value. In some sense, conventional transport equations for the mean quantities and evolution equations for the bulk surface-averaged quantities complement one another and offer an opportunity to explore flame-turbulence interaction from different perspectives. The former approach allows for variations within the mean flame brush, but does not address differences between the mean and bulk surface-averaged quantities, whereas the latter approach addresses the difference, but do not address the variations.

In addition to the major goal stated above, this work also pursues two other closely related, supplementary goals. First, certain terms in the derived evolution equations are singular in the so-called zero-gradient points [48], i.e., points where $|\nabla c|(\boldsymbol{x}, t) = 0$, but $0 < c(\boldsymbol{x}, t) < 1$. Such points can appear when an isosurface becomes too complicated to stay "regular," i.e., to have a finite curvature everywhere and to have no self-intersections, critical points, or edges [18]. While the zero-gradient points can appear during collisions of locally planar reaction waves in moderate and even weak turbulence, they are much more expected in highly turbulent reacting flows. Accordingly, applicability of the derived evolution equations to analyzing DNS data obtained from highly turbulent reaction waves will be addressed in this paper.

Second, surface-averaged quantities can be evaluated using different methods. On the one hand, following Veynante and Vervisch [16], we can define an instantaneous area-weighted surface average as follows:

$$\langle\phi\rangle_{s}|_{\hat{c},t} \equiv \overline{\phi|\nabla c|\delta(c-\hat{c})} \,/\, \overline{|\nabla c|\delta(c-\hat{c})}. \tag{2}$$

Here, $\hat{c}$ is a reference value of the reaction progress variable on an isosurface, $\delta(c-\hat{c})$ is Dirac delta function, and $\overline{q}$ designates a value of an arbitrary quantity q, obtained by sequentially taking both ensemble and volume averages of q, i.e., $\overline{q} \equiv \lim_{M\to\infty} \frac{1}{M}\sum_{i=1}^{M} \frac{1}{|V|}\iiint_V q_{(i)}(\boldsymbol{x}, t)\, d\boldsymbol{x}$, where M is the number of realizations in the ensemble, $q_{(i)}$ pertains to the ith realization, and $|V|$ is the volume of the considered three-dimensional (3D) domain V characterized by $\varepsilon < c(\boldsymbol{x}, t) < 1-\varepsilon$. While the choice of $\varepsilon \ll 1$ affects the magnitude of $|V|$, the latter value does not affect the magnitude of $\langle\phi\rangle_{s}|_{\hat{c},t}$, because $|V|$ in the nominator of Eq. (2) and $|V|$ in the denominator cancel one another.

On the other hand, unweighted surface-averaged quantities can be defined by removing $|\nabla c|$ from the numerator and denominator in Eq. (2). Then,

$$\langle\phi\rangle_{v}|_{\hat{c},t} \equiv \overline{\phi\delta(c-\hat{c})} \,/\, \overline{\delta(c-\hat{c})}. \tag{3}$$

Unweighted surface-averaged quantities appear to be addressed in experimental papers aiming at evaluation of, e.g., local flame thickness [49–55] by measuring $|\nabla c|$, local flame curvature κ [54–57], or local strain rate a_t [58].

In spite of the wide use of surface-averaged quantities, the method applied to extract them from DNS data is rarely discussed in detail and the difference in area-weighted and unweighted values of the same surface-averaged quantity ϕ is often disregarded implicitly, leading to potential ambiguity. While the two definitions given by Eqs. (2) and (3) are different and results of applications of the two equations are also expected to be different, the present authors are not aware on a target-directed research into the issue and, in particular, on a discussion of effects that could stem from the difference.

Therefore, this work aims at filling this gap by comparing differently defined surface-averaged quantities and relevant evolution equations in order to show that the difference referred to is of fundamental importance. For instance, as will be argued later, such a difference should be taken into account when discussing an apparent physical paradox, i.e., contradiction between data [49,50,59] that indicate thinning of local reaction waves in turbulent flows and data [40,51,55,60–63] that show the opposite effect. A detailed review of relevant experimental and DNS data can be found elsewhere [63,64].

Following the one major and two supplementary goals stated above, relations between area-weighted and unweighted surface-averaged quantities are discussed in Sec. II. Subsequently, in the same section, a general method for deriving evolution equations for bulk surface-averaged quantities is developed and such evolution equations are derived for FSD $|\nabla c|$, local thickness $1/|\nabla c|$, and displacement speed S_d, starting from transport equations for these quantities. In this regard, it is worth noting that while transport equations for $|\nabla c|$ and $1/|\nabla c|$ are well known, derivation of a transport equation for S_d appears to be a different result. In Sec. III, the numerical

approach used to evaluate various terms in the derived evolution equations is described and the simulation conditions are reported. Results of the simulations are discussed in Sec. IV, which aims at showing that (i) the difference between area-weighted and unweighted surface-averaged quantities can be of fundamental importance and (ii) all terms in the derived evolution equations can be extracted with good precision from DNS data obtained from highly turbulent reacting flows. Conclusions are summarized in Sec. V. Appendices A–C and D supplement the analysis performed in Sec. II and the information provided in Sec. IV, respectively.

II. ANALYSIS

A. Differently defined surface-averaged quantities

Equations (2) and (3) result straightforwardly in the following relations:

$$\langle\phi\rangle_s = \langle\phi|\nabla c|\rangle_v / \langle|\nabla c|\rangle_v, \tag{4}$$

$$\langle\phi\rangle_v = \langle\phi/|\nabla c|\rangle_s \langle|\nabla c|\rangle_v \tag{5}$$

between area-weighted and unweighted surface-averaged values of the quantity ϕ.

Accordingly, the difference between area-weighted and unweighted surface averages is

$$\langle\phi\rangle_s - \langle\phi\rangle_v = R_{\phi,|\nabla c|}|_v \frac{\langle\phi'^2\rangle_v^{1/2}\langle|\nabla c|'^2\rangle_v^{1/2}}{\langle|\nabla c|\rangle_v}, \tag{6}$$

where

$$R_{\phi,|\nabla c|}|_v \equiv \frac{\langle\phi'|\nabla c|'\rangle_v}{\langle\phi'^2\rangle_v^{1/2}\langle|\nabla c|'^2\rangle_v^{1/2}} \tag{7}$$

designates the correlation between ϕ and $|\nabla c|$, the prime symbol represents fluctuations within the unweighted framework, i.e.,

$$\phi' \equiv \phi - \langle\phi\rangle_v, \tag{8}$$

and $\langle\phi'^2\rangle_v^{1/2}$ is the standard deviation of ϕ within the same framework.

From the physical perspective, differences in $\langle|\nabla c|\rangle_s$ and $\langle|\nabla c|\rangle_v$ stem from variations of $|\nabla c|(\boldsymbol{x}, t)$ along the considered isosurface. Such variations are caused by perturbations of the local reaction wave structure by turbulent eddies and, hence, appear to be of minor importance in weakly turbulent $[u'/S_L \sim O(1)]$ flows. On the contrary, in a highly turbulent $(u' \gg S_L)$ flow, the perturbations and variations are expected to be significant.

Equation (6) shows that the difference in area-weighted and unweighted values can vanish either in an unlikely case of zero correlation between ϕ and $|\nabla c|$ or in the trivial case of zero fluctuations, i.e., $\langle\phi'^2\rangle_v^{1/2} = 0$. If $\phi = |\nabla c|$, then $\langle|\nabla c|\rangle_s - \langle|\nabla c|\rangle_v = \langle|\nabla c|'^2\rangle_v / \langle|\nabla c|\rangle_v \geqslant 0$ because $R_{|\nabla c|,|\nabla c|} = 1$. If $\phi = b/|\nabla c|$, where b is a positive constant, the difference $\langle b/|\nabla c|\rangle_s - \langle b/|\nabla c|\rangle_v \leqslant 0$ due to negative correlation of $R_{\frac{b}{|\nabla c|},|\nabla c|} \leqslant 0$ by virtue of Cauchy-Schwartz inequality.

Using these inequalities and applying Eq. (5) to $\phi = 1$, we arrive at

$$\frac{1}{\langle|\nabla c|\rangle_s} \leqslant \frac{1}{\langle|\nabla c|\rangle_v} = \left\langle\frac{1}{|\nabla c|}\right\rangle_s \leqslant \left\langle\frac{1}{|\nabla c|}\right\rangle_v. \tag{9}$$

Therefore, if the local wave thickness is characterized with a surface-averaged value of $|\nabla c|$ or $1/|\nabla c|$, then, results of evaluation of the area weighted $\langle|\nabla c|\rangle_s$ or $\langle 1/|\nabla c|\rangle_s$, respectively, which are often obtained when processing DNS data, are associated with a smaller thickness when compared to results found for the unweighted $\langle|\nabla c|\rangle_v$ or $\langle 1/|\nabla c|\rangle_v$, respectively, with the latter quantities being more relevant to experiments. This difference should be borne in mind when qualitatively comparing published data on the thickness. This difference is unlikely to be the sole cause of opposite trends reported for the influence of turbulence on the local reaction-wave thickness, but this difference can contribute to the inconsistency of the reported trends.

Definitions of the area-weighted and unweighted surface-averaged quantities, given by Eqs. (2) and (3), can be introduced in another form, by removing Dirac delta function in Eq. (2) using the following identity [65–67]:

$$\iiint_V \phi|\nabla c|\delta(c - \hat{c})\, d\boldsymbol{x} = \iint_{S|_{\hat{c},t}} \phi\, ds. \tag{10}$$

Then, the area-weighted surface-averaged values can be evaluated as follows:

$$\langle\phi\rangle_s|_{\hat{c},t} = \frac{\widehat{\iint_{S|_{\hat{c},t}} \phi\, ds}}{\widehat{\iint_{S|_{\hat{c},t}} ds}} = \frac{\widehat{\iint_{S|_{\hat{c},t}} \phi\, ds}}{\widehat{A|_{\hat{c},t}}}. \tag{11}$$

Here, $S|_{\hat{c},t}$ designates the isosurface of $c(\boldsymbol{x}, t) = \hat{c}$, whose total area is equal to

$$A|_{\hat{c},t} \equiv \iint_{S|_{\hat{c},t}} ds, \tag{12}$$

and the long-hat operator over any expression ψ represents the ensemble-averaged value of ψ, i.e., $\widehat{\psi} \equiv \lim_{M\to\infty} \frac{1}{M}\sum_{i=1}^{M} \psi_{(i)}$. Consequently, the volume and ensemble-averaged value $\overline{\psi}$ is equal to $(1/|V|)\widehat{\iiint_V \psi\, d\boldsymbol{x}}$.

To study the evolution of $\langle\phi\rangle_s|_{\hat{c},t}$, one can rewrite Eq. (11) as follows:

$$\widehat{A|_{\hat{c},t}\langle\phi\rangle_s|_{\hat{c},t}} = \widehat{\iint_{S|_{\hat{c},t}} \phi\, ds} \tag{13}$$

and take the time derivative of the right-hand side (rhs) and the left-hand side (lhs) of this equality. The derivation will be performed in Sec. II C, but before doing so, it is worth to briefly summarize well-known equations, which constitute the basis of the subsequent analysis.

B. Basic equations

Let us consider a reaction wave described by the following convection-diffusion-reaction equation:

$$\frac{\partial c}{\partial t} + \boldsymbol{u}\cdot\nabla c = \mathbb{D} + \mathbb{W}, \tag{14}$$

where t, $\boldsymbol{u}$, $\mathbb{D}$, and $\mathbb{W}$ designate time, flow velocity vector, diffusion term, and reaction rate, respectively. In the case

of a single reaction, the two terms on the rhs read as $\mathbb{D} = \nabla \cdot (\rho \mathcal{D} \nabla c)/\rho$ and $\mathbb{W} = W/\rho$, where $\mathcal{D}$ is the molecular diffusivity of c and W is the mass rate of product creation.

By (i) excluding zero-gradient points from consideration, (ii) defining the unit normal vector $\boldsymbol{n}$, the local displacement speed S_d, and the "total flame speed" $\boldsymbol{u}^*$ [19] using the following three equations,

$$\boldsymbol{n} \equiv \frac{\nabla c}{|\nabla c|}, \tag{15}$$

$$S_d \equiv \frac{\mathbb{D} + \mathbb{W}}{|\nabla c|}, \tag{16}$$

$$\boldsymbol{u}^* \equiv \boldsymbol{u} - \boldsymbol{n} S_d, \tag{17}$$

respectively, and (iii) introducing the "convective derivative based on the total flame speed" [19]

$$\frac{\partial^*}{\partial^* t}\phi \equiv \frac{\partial}{\partial t}\phi + \boldsymbol{u}^* \cdot \nabla \phi, \tag{18}$$

which is taken following an isosurface of $c(\boldsymbol{x}, t) = \hat{c}$; Eq. (14) can be rewritten in a "kinematic" form

$$\frac{\partial c}{\partial t} + \boldsymbol{u} \cdot \nabla c = S_d |\nabla c| \tag{19}$$

or

$$\frac{\partial^*}{\partial^* t} c = 0, \tag{20}$$

which is trivial, because any point on the isosurface always retain the same value of $c(\boldsymbol{x}, t) = \hat{c}$.

It is worth stressing that, as the displacement speed is defined by Eq. (16), the right-hand sides of Eqs. (14) and (19) are equal to one another and both equations are equivalent in a spatial domain where $|\nabla c|(\boldsymbol{x}, t) > 0$ (effects caused by appearance of zero-gradient points are addressed in the numerical part of this work). Both equations describe evolution of the entire $c(\boldsymbol{x}, t)$ field (i.e., a reaction wave of a finite thickness) and, for each isosurface of $c(\boldsymbol{x}, t) = \hat{c}$ within the field, the displacement speed S_d has a clear physical meaning: it is the speed of the isosurface with respect to the local flow. Moreover, $S_d(\boldsymbol{x}, t)$ is of fundamental value because it is an important component of the local stretch rate [see Eq. (1)], which controls the rate of change of the local isosurface area [17–20]. Therefore, while Eq. (19) looks similar to the level-set equation [68], the two equations are fundamentally different provided that S_d is given by Eq. (16). If another model expression for S_d, e.g., $S_d = S_L - \mathrm{Ma}\delta_L \mathcal{K}$ where δ_L is the laminar wave thickness and Ma is a Markstein number [17,28], is substituted into Eq. (19), then, the basic properties of the obtained kinematic equation can fundamentally differ from the basic properties of the second-order Eq. (14) [69–71], but such a case is not relevant to this study, which deals with Eq. (16).

C. Derivation of a general evolution equation for surface-averaged quantity

To take the time derivatives of various terms in Eq. (13), let us substitute $\boldsymbol{G} = \boldsymbol{n}\phi$ into the following transport theorem [19]:

$$\frac{d}{dt}\iint_{S(t)} \boldsymbol{G} \cdot \boldsymbol{n}\, ds = \iint_{S(t)} \Big[\frac{\partial}{\partial t}\boldsymbol{G} + (\boldsymbol{u}^* \cdot \nabla)\boldsymbol{G} - (\boldsymbol{G} \cdot \nabla)\boldsymbol{u}^* + \boldsymbol{G}\nabla \cdot \boldsymbol{u}^*\Big] \cdot \boldsymbol{n}\, ds. \tag{21}$$

We arrive at

$$\begin{aligned}\frac{d}{dt}\iint_{S_{|\hat{c},t}} \phi\, ds &= \iint_{S_{|\hat{c},t}} \Big[\frac{\partial}{\partial t}(\boldsymbol{n}\phi) + (\boldsymbol{u}^* \cdot \nabla)(\boldsymbol{n}\phi) - \phi(\boldsymbol{n} \cdot \nabla)\boldsymbol{u}^* + (\boldsymbol{n}\phi)\nabla \cdot \boldsymbol{u}^*\Big] \cdot \boldsymbol{n}\, ds \\ &= \iint_{S_{|\hat{c},t}} \Big[\frac{\partial}{\partial t}\phi + \boldsymbol{u}^* \cdot \nabla\phi\Big] ds + \iint_{S_{|\hat{c},t}} \big[-\boldsymbol{n}\boldsymbol{n} : \nabla \boldsymbol{u}^* + \nabla \cdot \boldsymbol{u}^*\big]\phi\, ds \\ &= \iint_{S_{|\hat{c},t}} \frac{\partial^*}{\partial^* t}\phi\, ds + \iint_{S_{|\hat{c},t}} \phi \mathcal{K}\, ds. \end{aligned} \tag{22}$$

Combining this equation written for $\phi = 1$ with the definition of the area-weighted, surface-averaged stretch rate, given by Eq. (11), and taking ensemble average, we arrive at

$$\langle \mathcal{K} \rangle_s = \frac{1}{\widehat{A}} \frac{\partial}{\partial t}\widehat{A}. \tag{23}$$

Henceforth, the symbol of partial derivative is used to stress that bulk surface-averaged quantities like $\widehat{A}_{\hat{c},t}$ depend not only on time, but also on $\hat{c}$, but subscript $\hat{c}, t$ is skipped for brevity.

Equations (13) and (23) allow us to easily derive an evolution equation for the area-weighted surface-averaged value $\langle \phi \rangle_s$ of the quantity ϕ. Indeed, differentiation of the former equation with respect to time yields

$$\widehat{A}\frac{\partial \langle \phi \rangle_s}{\partial t} + \langle \phi \rangle_s \frac{\partial \widehat{A}}{\partial t} = \widehat{\iint_S \frac{\partial^* \phi}{\partial^* t} ds} + \widehat{\iint_S \phi \mathcal{K}\, ds} \tag{24}$$

using Eq. (22). Finally, dividing the rhs and the lhs of Eq. (24) with $\widehat{A}$ and using Eqs. (11) and (23), we arrive at the following general evolution equation for the bulk area-weighted surface-averaged value of the quantity ϕ:

$$\frac{\partial \langle \phi \rangle_s}{\partial t} = \left\langle \frac{\partial^*}{\partial^* t}\phi \right\rangle_s + \langle \phi \mathcal{K} \rangle_s - \langle \phi \rangle_s \langle \mathcal{K} \rangle_s. \tag{25}$$

The derived evolution equation (25) holds (i) for an arbitrary quantity ϕ, (ii) for any isosurface of $c(\boldsymbol{x}, t) = \hat{c}$ with $\hat{c} \in (0, 1)$, and (iii) for any time instant t. An evolution equation for the second moment of conditioned fluctuation is derived in Appendix A.

Equation (25) directly shows that the time derivative of the bulk area-weighted surface-averaged quantity $\langle \phi \rangle_s(t)$ (see the lhs) differs from the bulk area-weighted time derivative of $\phi(\boldsymbol{x}, t)$, taken by following the surface (see the rhs). The difference between the two time derivatives is controlled by the bulk area-weighted correlation between ϕ and the stretch rate $\mathcal{K}$. Therefore, evaluation of all surface-averaged terms on the rhs of a transport equation for $\phi(\boldsymbol{x}, t)$ does not allow us to study the evolution of $\langle \phi \rangle_s$ because the sum of the local and instantaneous rhs terms is equal to $\frac{\partial^*}{\partial^* t}\phi$ at any point at

any instant, but the surface averaged $\langle \frac{\partial^*}{\partial^* t}\phi \rangle_s$ does not equal to the time derivative of $\langle \phi \rangle_s$. The point is that a statistical subensemble that the surface average is taken over depends on $\boldsymbol{x}$ and t due to the random motion of the surface. Thus, there is fundamental need for studying evolution equations for various $\langle \phi \rangle_s$, but this task has not yet been addressed in the combustion literature, to the best of the present authors' knowledge.

D. Particular evolution equations for surface-averaged quantities

If we know a transport equation for $\phi(\boldsymbol{x}, t)$, then the evolution equation for $\langle \phi \rangle_s$ can simply be obtained by substituting the transport equation into the first term on the rhs of Eq. (25). Let us consider some particular examples.

Using the following well-known transport equation

$$\frac{1}{|\nabla c|}\frac{\partial^*}{\partial^* t}|\nabla c| = \mathcal{K} + \nabla \cdot (S_d \boldsymbol{n}) - \nabla \cdot \boldsymbol{u} \tag{26}$$

for FSD [18,19], which is derived in Appendix B for completeness, we arrive at

$$\frac{\partial}{\partial t}\langle |\nabla c| \rangle_s = 2\langle |\nabla c| \mathcal{K} \rangle_s + \langle |\nabla c| \nabla \cdot (S_d \boldsymbol{n}) \rangle_s - \langle |\nabla c| \nabla \cdot \boldsymbol{u} \rangle_s - \langle |\nabla c| \rangle_s \langle \mathcal{K} \rangle_s \tag{27}$$

and

$$\frac{\partial}{\partial t}\left\langle \frac{1}{|\nabla c|} \right\rangle_s = -\left\langle \frac{1}{|\nabla c|} \nabla \cdot (S_d \boldsymbol{n}) \right\rangle_s + \left\langle \frac{1}{|\nabla c|} \nabla \cdot \boldsymbol{u} \right\rangle_s - \left\langle \frac{1}{|\nabla c|} \right\rangle_s \langle \mathcal{K} \rangle_s \tag{28}$$

because $\partial |\nabla c|^{-1}/\partial t = -|\nabla c|^{-2}\partial |\nabla c|/\partial t$. The former and latter equations describe evolutions of the bulk area-weighted surface-averaged FSD and local flame thickness, respectively.

It is worth stressing that the area-weighted thickness $\langle 1/|\nabla c| \rangle_s = 1/\langle |\nabla c| \rangle_v$ [see Eq. (9)] and, consequently, it is unlikely to be notably affected by zero-gradient points. On the contrary, the unweighted thickness $\langle 1/|\nabla c| \rangle_v$ can be affected by very large local values of $1/|\nabla c|(\boldsymbol{x}, t)$ in the vicinity of such points. Accordingly, the former thickness $\langle 1/|\nabla c| \rangle_s$ appears to be substantially more robust when compared to $\langle 1/|\nabla c| \rangle_v$.

Using the equality $\langle 1/|\nabla c| \rangle_s$ and $1/\langle |\nabla c| \rangle_v$ and substituting $1/|\nabla c|$, $\nabla \cdot (S_d \boldsymbol{n})/|\nabla c|$, and $\nabla \cdot \boldsymbol{u}/|\nabla c|$ into Eq. (4), the evolution equation (28) for the bulk area-weighted surface-averaged flame thickness $\langle 1/|\nabla c| \rangle_s$ can be rewritten in the form of an evolution equation for the bulk unweighted surface-averaged FSD

$$\frac{1}{\langle |\nabla c| \rangle_v}\frac{\partial}{\partial t}\langle |\nabla c| \rangle_v = \frac{\partial}{\partial t}\ln \langle |\nabla c| \rangle_v = \langle \mathcal{K} \rangle_s + \langle \nabla \cdot (S_d \boldsymbol{n}) \rangle_v - \langle \nabla \cdot \boldsymbol{u} \rangle_v = \langle \mathcal{K} \rangle_s - \langle \nabla \cdot \boldsymbol{u}^* \rangle_v. \tag{29}$$

Since $\langle 1/|\nabla c| \rangle_s = 1/\langle |\nabla c| \rangle_v$, Eqs. (28) and (29) describe the evolution of the same quantity, but are written in different forms. In the following, the latter, more compact equation will be used. It is worth remembering that one term, i.e., $\langle \mathcal{K} \rangle_s$, on the rhs of Eq. (29) is area weighted, whereas other terms, i.e., $\langle \nabla \cdot \boldsymbol{u} \rangle_v$ and $\langle \nabla \cdot (S_d \boldsymbol{n}) \rangle_v$ or their difference $\langle \nabla \cdot \boldsymbol{u}^* \rangle_v$, are unweighted.

Application of the area-weighted surface average to the rhs of the transport equation (26) multiplied with $|\nabla c|$ and to the counterpart transport equation for the thickness $1/|\nabla c|(\boldsymbol{x}, t)$ allows us to compare the surface-averaged transport equations with the newly derived evolution equations for the bulk surface-averaged quantities. For the FSD $|\nabla c|$, the area-weighted surface-averaged rhs of Eq. (26) multiplied with $|\nabla c|$ differs clearly from the rhs of Eq. (27) because the latter equation involves a correlation of the surface averaged $\mathcal{K}$ and $|\nabla c|$. The unweighted surface-averaged rhs of Eq. (26) multiplied with $|\nabla c|$ looks almost similar to the rhs of Eq. (29), but the stretch rate in the latter equation is area weighted. As will be shown later, $\langle \mathcal{K} \rangle_s$ differs significantly from $\langle \mathcal{K} \rangle_v$ and substitution of the former quantity with the latter one yields large errors in a highly turbulent reaction wave (see Figs. 4 and 5 in Sec. IV).

For the thickness $1/|\nabla c|$, the surface-averaged rhs of the transport equation (26) multiplied with $|\nabla c|^{-1}$ looks almost similar to the rhs of Eq. (28), but the latter rhs involves a product of $\langle \frac{1}{|\nabla c|} \rangle_s$ and $\langle \mathcal{K} \rangle_s$, contrary to $\langle \frac{1}{|\nabla c|}\mathcal{K} \rangle_s$ on the former rhs.

Thus, simple application of a surface-averaged operator to both sides of a transport equation for ϕ does not allow us to explore evolution of the surface averaged ϕ. As already noted, differences between evolutions of mean and conditioned (e.g., surface-averaged) quantities stem from the fact that a statistical subensemble that the surface average is taken over depends on $\boldsymbol{x}$ and t due to the random motion of the surface.

A common feature of the transport equation (26) and the evolution equations (27)–(29) is as follows. The evolutions of both FSD $|\nabla c|$ and thickness $1/|\nabla c|$ are controlled by a balance of appropriately averaged stretch rate $\mathcal{K}$, self-propagation term $\nabla \cdot (S_d \boldsymbol{n})$, and dilatation $\nabla \cdot \boldsymbol{u}$. In the case of a constant density ($\nabla \cdot \boldsymbol{u} = 0$) and a material surface ($S_d = 0$), the evolutions are solely controlled by turbulent strain rate ($\mathcal{K} = a_t$ in this case), in line with Batchelor's classical result [72]. Contributions of the aforementioned terms to the evolutions of various surface averaged $|\nabla c|$ and $1/|\nabla c|$ will be discussed in a followup paper [73]. Here, we restrict ourselves to noting that the stretch-rate (self-propagation) terms work to increase (decrease, respectively) $|\nabla c|$ and make the flame thinner (thicker, respectively), whereas the dilatation terms play a minor role in developing highly turbulent flames.

Finally, the following evolution equation for the bulk area-weighted surface-averaged displacement speed,

$$\frac{\partial}{\partial t}\langle S_d \rangle_s = -\langle S_d \nabla \cdot (S_d \boldsymbol{n}) \rangle_s + \langle S_d \nabla \cdot \boldsymbol{u} \rangle_s - \langle S_d \rangle_s \langle \mathcal{K} \rangle_s - 2\left\langle \mathcal{D}\frac{\nabla \nabla c : \nabla \boldsymbol{u}}{|\nabla c|} \right\rangle_s + \langle \mathcal{D}\boldsymbol{n} \cdot \nabla^2 (S_d \boldsymbol{n}) \rangle_s + 2\left\langle \mathcal{D}\frac{\nabla \nabla c : \nabla (S_d \boldsymbol{n})}{|\nabla c|} \right\rangle_s - \langle \mathcal{D}\boldsymbol{n} \cdot \nabla^2 \boldsymbol{u} \rangle_s, \tag{30}$$

can be obtained using a transport equation for S_d, newly derived in Appendix C under conditions of a constant diffusivity and a reaction rate depending solely on c. Note that

substitution of Eq. (16) in the nominator of Eq. (2) shows that $\langle S_d \rangle_s = \langle \mathbb{D} + \mathbb{W} \rangle_v / \langle |\nabla c| \rangle_v$. Consequently, appearance of zero-gradient points is not associated with potential singularity of $\langle S_d \rangle_s$, but could make the bulk unweighted surface-averaged displacement speed $\langle S_d \rangle_v$ unbounded. However, the latter quantity is not addressed in this paper.

As far as the rhs of Eq. (30) is concerned, the first, fifth, and sixth terms could potentially be unbounded. Accordingly, this evolution equation is of particular interest for investigating the numerical robustness of the developed approach in the vicinity of zero-gradient points.

E. Relations for statistically stationary surface-averaged quantities

By definition, when a reaction wave evolves into a statistically stationary state (denoted as t_∞ in the following), the time derivative of any statistical quantity becomes zero, i.e., $\partial_t \langle \phi \rangle_s |_{\hat{c},t_\infty} = 0$ and $\partial_t \langle \phi \rangle_v |_{\hat{c},t_\infty} = 0$, $\forall\, \hat{c} \in (0, 1)$. Moreover, due to Eq. (23) the fully developed mean stretch rate must vanish, i.e.,

$$\langle \mathcal{K} \rangle_s |_{\hat{c},t_\infty} = 0. \tag{31}$$

Consequently, Eq. (27) reduces to

$$\begin{aligned} &2\langle |\nabla c| \mathcal{K} \rangle_s |_{\hat{c},t_\infty} \\ &\quad = -\langle |\nabla c| \nabla \cdot (S_d \boldsymbol{n}) \rangle_s |_{\hat{c},t_\infty} + \langle |\nabla c| \nabla \cdot \boldsymbol{u} \rangle_s |_{\hat{c},t_\infty} \end{aligned} \tag{32}$$

$\forall\, \hat{c} \in (0, 1)$ at t_∞. Similarly, Eq. (29) reads as

$$\langle \nabla \cdot (S_d \boldsymbol{n}) \rangle_v |_{\hat{c},t_\infty} - \langle \nabla \cdot \boldsymbol{u} \rangle_v |_{\hat{c},t_\infty} = 0. \tag{33}$$

Finally, Eq. (30) reduces to

$$\begin{aligned} &\langle S_d \nabla \cdot (S_d \boldsymbol{n}) \rangle_s |_{\hat{c},t_\infty} - \langle S_d \nabla \cdot \boldsymbol{u} \rangle_s |_{\hat{c},t_\infty} \\ &\quad = -2\mathcal{D} \left\langle \frac{\nabla \nabla c : \nabla \boldsymbol{u}}{|\nabla c|} \right\rangle_s \Big|_{\hat{c},t_\infty} + \mathcal{D} \langle \boldsymbol{n} \cdot \nabla^2 (S_d \boldsymbol{n}) \rangle_s |_{\hat{c},t_\infty} \\ &\qquad + 2\mathcal{D} \left\langle \frac{\nabla \nabla c : \nabla (S_d \boldsymbol{n})}{|\nabla c|} \right\rangle_s \Big|_{\hat{c},t_\infty} - \mathcal{D} \langle \boldsymbol{n} \cdot \nabla^2 \boldsymbol{u} \rangle_s |_{\hat{c},t_\infty}. \end{aligned} \tag{34}$$

III. COMPUTATIONAL SETUP

One of the major goals of the numerical part of this paper is to study whether or not the three evolution equations for surface-averaged quantities derived above, i.e., Eqs. (27), (29), and (30), are applicable to explore heavily disturbed turbulent reaction waves. For this purpose, these equations are applied to analyze a representative highly turbulent case (case C in the following) selected from a large DNS database computed earlier [14,15,74–79].

The above task is motivated by eventual appearance of zero-gradient points in highly turbulent reacting waves, as already discussed in Sec. I. In numerical simulations, the probability of appearance of such points in nodes of a discrete mesh is negligible. Nevertheless, specific care should be taken in the vicinity of zero-gradient points, where ϕ can unboundedly grow, thus, making surface-averaged quantities unbounded. To address issues associated with appearance of zero-gradient points, two supplementary cases A and B were designed and simulated, as discussed in Sec. III B. Evaluation of surface-averaged quantities in the vicinity of such points is further discussed in Appendix B to a recent paper [80].

In our earlier DNS's [14,15,76–79], propagation of a statistically one-dimensional (1D), planar, single-reaction wave in a homogeneous, isotropic, statistically stationary forced turbulence was simulated in the case of a dynamically passive wave, i.e., a wave that did not change the fluid density and viscosity, therefore, did not affect turbulence. The invoked simplifications allowed us to sample better statistics, as will be discussed later, and to investigate a large number of substantially different cases. Moreover, the simplifications significantly facilitate analyzing and interpreting the DNS data.

Although the above derivation of evolution equations was performed in the case of variable density, the equations are mainly kinematic in their nature. Accordingly, while thermal expansion effects play an important role in premixed turbulent combustion, as reviewed elsewhere [81,82], they seem to be of secondary importance for the derived evolution equations. Indeed, an analysis of other DNS data obtained from single-step and complex-chemistry premixed turbulent flames, performed in a followup work, indicates a minor influence of thermal expansion on the evolution of the bulk surface-averaged FSD and thickness $1/|\nabla c|$ in developing highly turbulent ($u' \gg S_L$) flames, i.e., the magnitudes of the dilatation terms are significantly less than the magnitudes of other terms in Eqs. (27) and (29) under such conditions [73]. Therefore, numerical results reported in the following appear to be relevant not only to constant-density turbulent reacting flows, but also to premixed flames. It is also worth remembering that recent results obtained by Dopazo *et al.* [20] in DNS studies of wave propagation in turbulent flows advanced fundamental understanding of turbulent premixed flames also.

A. DNS database

Since the DNS attributes are discussed in detail elsewhere [14,15,74–79], we will restrict ourselves to a very brief summary of the simulations.

The propagation of a single-reaction wave is governed by the following well-known convection-reaction-diffusion equation

$$\frac{\partial c}{\partial t} + \mathbf{u} \cdot \nabla c = \mathcal{D} \nabla^2 c + W, \tag{35}$$

which is a simplified form of Eq. (14) with $\mathbb{D} = \mathcal{D}\nabla^2 c$ and $\mathbb{W} = W$ and is widely used to model premixed combustion. In particular, Eq. (35) is the cornerstone equation of the laminar flame theory [83,84]. Here,

$$W = \frac{1}{1+\tau} \frac{1-c}{\tau_R} \exp\left[-\frac{Ze(1+\tau)^2}{\tau(1+\tau c)} \right] \tag{36}$$

is the reaction rate, τ_R is a constant reaction timescale, $\tau = 6$, and $Ze = 6$ in order for the rate W to depend on c in a highly nonlinear manner. As discussed in detail elsewhere [78], Eq. (36) allows us to mimic the highly nonlinear behavior of the reaction rate in a flame by considering constant-density reacting flows. Before each DNS run, the values of the laminar wave speed S_L and thickness δ_L were set and the required values of $\mathcal{D}$ and the reaction timescale τ_R were determined

in presimulations of the planar 1D laminar reaction wave modeled by Eqs. (35) and (36). In line with the theory [83,84], $S_L \propto \sqrt{\mathcal{D}/\tau_R}$.

The wave propagates in a forced, homogeneous, and isotropic turbulence described by the Navier-Stokes equations

$$\frac{\partial \mathbf{u}}{\partial t} + (\mathbf{u}\cdot\nabla)\mathbf{u} = -\rho^{-1}\nabla p + \nu\nabla^2\mathbf{u} + \mathbf{f}, \qquad (37)$$

where p is the pressure, a vector function $\mathbf{f}$ is used to maintain turbulence intensity by applying energy forcing at low wave numbers [85], the density ρ and kinematic viscosity ν are constants, and, therefore, the flow is not affected by the wave propagation, as already stressed earlier.

The governing equations are solved using an in-house DNS solver [86] developed for low-Mach-number reacting flows. The solver uses a second order symmetrical Strang splitting method [87] for temporal integration. A sixth order center difference scheme is used for all terms containing spatial derivative with the exception of the convection term in Eq. (35), which is discretized with a fifth order weighted essentially nonoscillatory (WENO) scheme [88] to avoid numerical overshooting.

The wave evolves in a fully periodic rectangular box with size of $\Lambda_x \times \Lambda \times \Lambda$ represented using a uniform grid of $N_x \times N \times N$ cubic cells. The boundary conditions are periodic not only in transverse directions y and z, but also in direction x normal to the mean wave surface, as discussed in detail elsewhere [75–77].

An initial turbulence field is generated by synthesizing prescribed Fourier waves [89] with an initial rms velocity u_0 and the integral scale $\ell_0 = \Lambda/4$. The initial turbulent Reynolds number $\mathrm{Re}_0 = u_0\ell_0/\nu = 50$, 100, or 200 is changed by changing the domain width Λ. Subsequently, a nondecaying incompressible turbulent field is obtained by integrating Eq. (37). Implementation of the forcing scheme is discussed in detail in Sec. III in Ref. [76], where an expression for the forcing vector function $\mathbf{f}$ is reported [see Eq. (6) in the cited paper].

In all simulated turbulent cases, the turbulent velocity, length, and timescales showed statistically stationary behavior [74,75] at $t > t^* = 6000\Delta t > 3.5\tau_t^0$. Here, $\tau_t^0 = \ell_0/u'$ and $\Delta t = 0.028\Lambda/(Nu')$ is the time step of the simulations. Accordingly, the forced turbulence is characterized by quantities averaged over the computational domain and time at $t > t^*$. The generated turbulence is homogeneous (see Fig. 2 in Ref. [74]), isotropic (see Fig. 1 in Ref. [77]), and statistically stationary (see Fig. 2 in Ref. [76]), with volume-averaged values of u' or the dissipation rate of the turbulent energy being very close to u_0' or weakly oscillating around $1.6{u_0'}^3/\ell_0$, respectively (see Fig. 1 in Ref. [75]).

In this work, both fully developed and transient reaction waves are simulated. Following a common practice, the simulations of wave propagation start from the precomputed laminar-wave profile of $c_L(\xi)$ with $dc_L/d\xi > 0$. In order to study a fully developed turbulent reaction wave, a planar wave $c^s(x,0) = c_L(\xi)$ is initially ($t = 0$) released at $x_0 = \Lambda_x/2$ such that $\int_{-\infty}^{0} c_L(\xi)d\xi = \int_0^{\infty}[1 - c_L(\xi)]d\xi$ and $\xi = x - x_0$. Subsequently, evolution of this field $c^s(x,t)$ is simulated by solving Eq. (35). Computations of fully developed statistics with sampling every 100 time steps Δt are started after the forced turbulence has reached statistical stationary at $t = t^*$ and are performed over a time interval longer than $50\tau_t^0$.

In order to study transient turbulent reaction waves, the same precomputed laminar-wave profiles $c_L(\xi)$ are simultaneously embedded into the turbulent flow in $\mathcal{M}$ equidistantly separated planar zones centered around $x_m/\Lambda_x = (m - 0.5)/\mathcal{M}$, i.e., $c_m^t(x,t^*) = c_L(\xi_m)$, where coordinates $\xi_m = x - x_m$ are set using $\int_{-\infty}^{0} c_L(\xi_m)d\xi_m = \int_0^{\infty}[1 - c_L(\xi_m)]d\xi_m$ and m is an integer number ($1 \leqslant m \leqslant \mathcal{M} = 15$). Subsequently, evolutions of $\mathcal{M}$ transient fields $c_m^t(\mathbf{x},t)$ are simulated by solving $\mathcal{M}$ independent Eqs. (35), with these fields affecting neither each other nor turbulence in the studied case of $\rho =$ const and $\nu =$ const. Accordingly, all $\mathcal{M}$ transient fields $c_m^t(\mathbf{x},t)$ are independent from each other.

The transient simulations are run over $2\tau_t^0$ before being reset. Subsequently, at $t = t^* + 2j\tau_t^0$ with $1 \leqslant j \leqslant J$, the flow is again populated by $\mathcal{M}$ new profiles of $c_L(\xi_m)$ and the transient simulations are repeated. Therefore, the total duration of simulations is $t^* + 2J\tau_t^0$.

The time-dependent statistics for a time interval of $2\tau_t^0$ is computed by averaging the DNS data over the entire ensemble ($m = 1,\ldots,\mathcal{M}$) of $\mathcal{M}$ $c_m^t(\boldsymbol{x},t)$ fields and over J time intervals of $t^* + 2(j-1)\tau_t^0 \leqslant t \leqslant t^* + 2j\tau_t^0$, where $j = 1,\ldots,J$. Accordingly, the total number of realizations is equal to $M = \mathcal{M} \times J$. For comparison, the fully developed statistics computed using a single field of c^s is associated with $M = 2J\tau_t^0/(100\Delta t)$ realizations.

Such a method, i.e., simulations of $\mathcal{M}$ independent transient fields, significantly increases the sampling counts for calculating transient statistics and was already applied to studying self-propagation of an infinitely thin front [74,75] and a reaction wave of nonzero thickness [14,15,76–79] in homogeneous isotropic turbulence.

It is worth noting that the transient data not only are of interest in themselves, e.g., because the vast majority of premixed turbulent flames are developing flames, as discussed in detail elsewhere [23,90], but also offer an opportunity to control the following numerical issue. As noted earlier, zero-gradient points can appear in intense turbulence and $1/|\nabla c|$ or S_d can be unboundedly large in the close vicinity of such points. Since the transient waves $c_m^t(\boldsymbol{x},t) = \hat{c}$ begin their evolution from a regular flat initial surface, monitoring evolution of (i) isosurfaces of the transient fields $c_m^t(\boldsymbol{x},t) = \hat{c}$ and (ii) the relevant surface-averaged quantities offers an opportunity to detect any anomaly in the developing surface-averaged values of $1/|\nabla c|$ or S_d and to see eventual influence of zero-gradient points on various surface-averaged terms in the derived evolution equations.

B. Case setup

Various cases are set up by selecting one of forced turbulence fields and specifying the speed S_L and thickness $\delta_F = D/S_L$ of the laminar reaction wave, with the required reaction timescale τ_R in Eq. (36) being found in 1D precomputations of the laminar wave. Since the reaction waves are dynamically passive, the choice of a turbulent field is independent of the choice of S_L and δ_F.

Totally 45 cases characterized by the Damköhler number $\mathrm{Da} = \tau_t/\tau_F = 0.01$–$24.7$, the Karlovitz number $\mathrm{Ka} =$

TABLE I. Three representative DNS cases.

Case	$\frac{\Lambda_x}{\Lambda}$	N_x	$\frac{u_0}{S_L}$	$\frac{L_{11}}{\delta_F}$	$\frac{\delta_F}{\Delta x}$	Da	Ka	Pe
A	8	2048	5	5.3	24	1.07	0.94	27
B	1	1048	2	5.3	24	2.67	0.38	10.6
C	8	2048	60	1.2	24	0.02	390	69.5

$\tau_F/\tau_\eta = 0.36$–587, $u'/S_L = 0.5$–90, and $L_{11}/\delta_F = 0.39$–12.4 were simulated, with a few cases being designed to show weak sensitivity of computed results to grid resolution, Λ/L_{11}, etc. [76]. Here, $\tau_F = \delta_F/S_L$ is the wave timescale, $\tau_t = L_{11}/u'$ and $\tau_\eta = (\nu/\overline{\varepsilon})^{1/2}$ are integral and Kolmogorov, respectively, timescales of the turbulence, and $\overline{\varepsilon} = 2\nu\overline{S_{ij}S_{ij}}$ is the dissipation rate averaged over the computational domain and time $t > t^*$. All 45 cases and reasons for selecting them are discussed in detail elsewhere [76].

Since (i) the major goals of the numerical part of this work are (a) to show significant difference between area-weighted and unweighted surface-averaged quantities and (b) to assess the influence of zero-gradient points on the robustness of numerical evaluation of various terms in the derived evolution equations and (ii) both the difference and the influence are expected to be more pronounced in highly turbulent medium; let us restrict ourselves to results obtained in a single representative highly turbulent and well resolved case. Its major characteristics are reported on the bottom line (case C) in Table I, where $\mathrm{Pe} = u'L_{11}/\mathcal{D}$ is the turbulent Péclet number and a ratio of $\delta_F/\Delta x$ characterizes the grid resolution in terms of the number of grid points per the laminar wave thickness. Moreover, in case C, $L_{11}/\Lambda = 0.11$, $\tau_t^0/\tau_t = 2.3$, $\eta/\Delta x = 1.1$, $\mathrm{Re}_0 = 200$, and $\mathrm{Re}_\lambda = u'\lambda/\nu = 45$. Here, $\eta = (\nu^3/\overline{\varepsilon})^{1/4}$ is the Kolmogorov length scale and $\lambda = (15\nu u'^2/\overline{\varepsilon})^{1/2}$ is the Taylor length scale. More data can be found in Table I in an earlier paper [76], where 16 nondimensional characteristics of this case (case D4 therein) are reported. A 2D snapshot of the fully developed $c^s(\boldsymbol{x}, t)$ field simulated in this case is shown in Fig. 1.

To explore eventual influence of zero-gradient points and their neighborhoods on the evaluation of various terms in the derived evolution equations, two supplementary two-dimensional (2D) cases were designed. Case A is largely identical to case C, but the turbulent field is replaced with a frozen shear flow, i.e., $u(x, y, z, t) = -u_0 \cos(2\pi y/\Lambda)$, $v = w = 0$, and the momentum (37) is not solved. As shown in

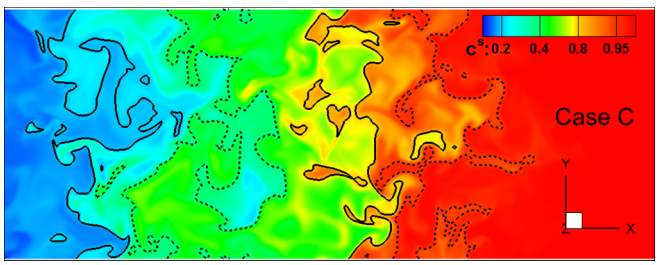

FIG. 1. A 2D snapshot of the fully developed c^s field in case C. Four (solid and dotted) black lines show isosurfaces of $c = 0.2$, 0.4, 0.8, and 0.95 from left to right.

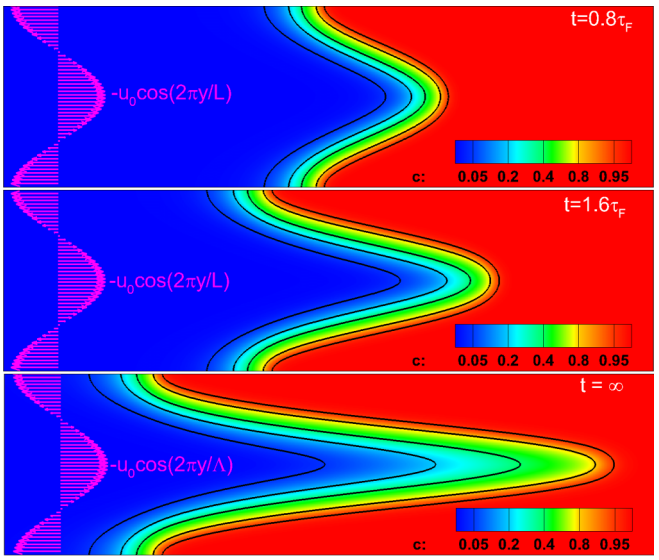

FIG. 2. Snapshots of the c field in case A at two transient instants of (a) $t = 0.8\tau_F$ and (b) $1.6\tau_F$ and (c) at the fully developed state of t_∞. Five black lines show isosurfaces of $c = 0.05$, 0.2, 0.4, 0.8, and 0.95 from left to right.

Fig. 2, isosurfaces are only bent in case A, but there is no zero-gradient point in the computational domain. Characteristics of case A, reported in Table I, are calculated using $L_{11} = \Lambda/2$, $u' = u_0$, and $t_\eta = t_\tau = L_{11}/u_0$. Case B is also based on a frozen velocity field, but the field is different, i.e., $u(x, y, z, t) = u''(x, y)$, $v(x, y, z, t) = v''(x, y)$, $w = 0$, and $\nabla \cdot \boldsymbol{u}'' = 0$. The field $\boldsymbol{u}''$ represents a 2D, zero-mean, spatially fluctuating velocity field generated using a reduced version of the method for synthesizing the initial 3D turbulence. Characteristics of case B, reported in Table I, are calculated by analyzing the 2D velocity field (u_0 and L_{11}) and using $\tau_\eta \approx \tau_t = L_{11}/u_0$ to evaluate Ka. As shown in Fig. 3, the design of case B aims at mimicking a moderately disturbed reaction wave passing through flow vortices and allowing appearance of a small number of zero-gradient points during collisions of reaction waves.

Thus, comparison of results computed in cases A (no zero-gradient points), B (a few zero-gradient points), and C (no restrictions on appearance of zero-gradient points) offers an opportunity to gain insight into the influence of such points on the evaluation of various terms in the derived evolution equations.

Some peculiarities of the transient simulations in cases A and B are described in Appendix D, where methods applied to evaluate surface-averaged quantities and various terms in the derived evolution equations are also discussed.

IV. RESULTS AND DISCUSSION

A. Residuals in the evolution equations

We used the DNS data to examine the evolution equations for three surface-averaged quantities Ψ. All these equations, i.e., Eq. (27) for $\Psi = \langle|\nabla c|\rangle_s|_{\hat{c},t}$, Eq. (29) for $\Psi = \ln\langle|\nabla c|\rangle_v|_{\hat{c},t}$, and Eq. (30) for $\Psi = \langle S_d\rangle_s|_{\hat{c},t}$, take the general

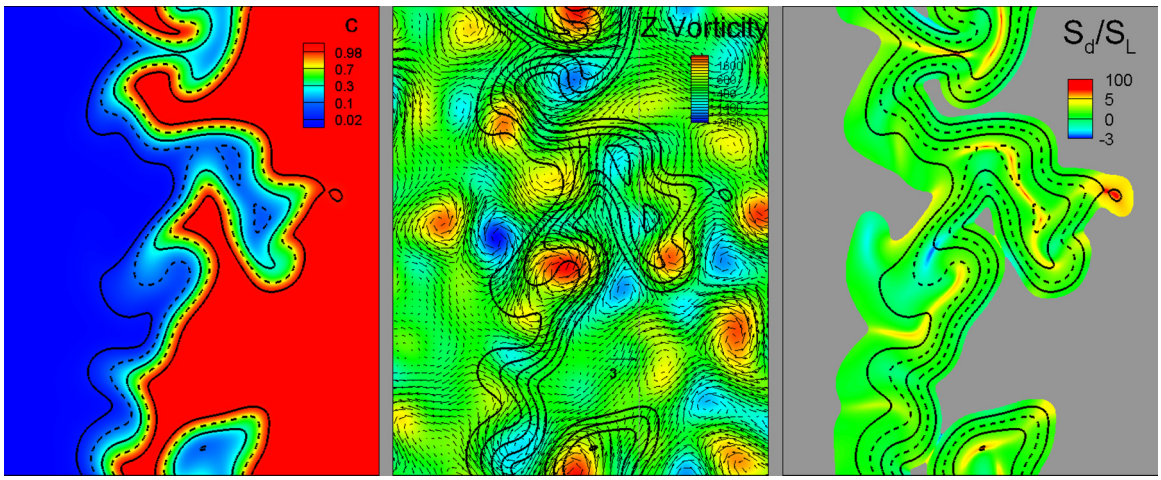

FIG. 3. Snapshots of the c, vorticity, and S_d fields in case B at a single representative instant. Only a part of the computational domain, which contains the most disturbed reaction wave is plotted. Four dashed and solid lines show the isosurfaces of $c = 0.02$, 0.1, 0,3 and 0.98, local velocity vectors are plotted with line arrows.

form

$$\frac{\partial}{\partial t}\Psi = \sum \text{rhs} \tag{38}$$

and should hold (i) for all isosurfaces of $c(\boldsymbol{x}, t) = \hat{c}$ such that $\hat{c} \in (0, 1)$ and also (ii) at all time instants t. In each simulated case (A, B, or C), the following three terms were computed: (a) the lhs term, i.e., the time derivative of Ψ, (b) the sum of all the rhs terms, i.e., $\sum$ rhs, and (c) the residual difference $\mathcal{R} \equiv \sum \text{rhs} - \frac{\partial}{\partial t}\Psi$.

The three aforementioned terms are compared using two sets of figures. The first set shows evolution of the above terms conditioned to two (or three) isosurfaces: $\hat{c} = 0.1$ associated with "mixing" zone (or "preheat" zone in flames), $\hat{c} = c^* = 0.88$ associated with the inner reaction zone [the reaction rate W given by Eq. (36) peaks at $\hat{c} = c^* = 0.88$ under conditions of the present simulations], and, sometimes, $\hat{c} = 0.5$, associated with the middle of the local reaction wave. Such data computed in cases A–C are plotted for $\Psi = \langle |\nabla c| \rangle_s$ in Fig. 4, for $\Psi = \ln \langle |\nabla c| \rangle_v$ in Fig. 6, and for $\Psi = \langle S_d \rangle_s$ in Fig. 8. In these figures, time t is normalized with $\tau_F^* = \tau_F$ in cases A and B or $\tau_F^* = \tau_t$ ($\approx \tau_F/22.5$) in case C.

The second set of figures shows dependence of the considered terms on the value of $\hat{c}$ the terms are conditioned to. Such dependencies are reported at three representative time instants t: an early instant $0.045\tau_F^*$, a middle instant $0.32\tau_F^*$, or $1.125\tau_F^*$, and the fully developed state t_∞. Such data computed in cases A–C are plotted for $\Psi = \langle |\nabla c| \rangle_s$ in Fig. 5, for $\Psi = \ln \langle |\nabla c| \rangle_v$ in Fig. 7, and for $\Psi = \langle S_d \rangle_s$ in Fig. 9.

For all three Eqs. (27), (29), and (30), the six aforementioned figures indicate a good match between the lhs term $\frac{\partial}{\partial t}\Psi$, shown in red dots, and the sum of rhs terms $\sum$ rhs, shown in blue open circles. Such a good match holds for almost all isosurfaces of $\hat{c} \in (0, 1)$ in all three cases at almost all time instants during a time interval of $0 < t < 2\tau_F^*$, as well as at t_∞. The residual terms $\mathcal{R}$ shown in black stars are sufficiently close to zero, with the exception of first two instants of data sampling in Figs. 4, 6, and 8. This mismatch between the lhs and rhs terms could be attributed to numerical errors when approximating $\frac{\partial}{\partial t}\Psi$ with the one-sided difference.

If the first two time instants are excluded from consideration, then the three equations do show nearly perfect zero residuals in the simplest laminar case A, which is associated with the lack of zero-gradient points. In the highly turbulent case C, small, but nonzero residuals are observed in Fig. 4(f) for Eq. (27) and in Figs. 8(g) and 8(i) and 9(h) for Eq. (30) during the late evolution stage. As discussed earlier, these residuals could be reduced by increasing the number of realizations (the shown data were obtained for $M = 750$) that were used for sampling transient statistics at later evolution stage, i.e., when a significant amount of zero-gradient points appeared on the heavily disturbed reaction-wave surface. The fact that the realization number for sampling the fully developed statistics ($M = 2249$) was significantly larger than the transient $M = 750$ can explain relatively small residuals observed in the aforementioned figures at t_∞.

In order to quantify the residuals, a ratio $\mathcal{R}_N$ of $|\mathcal{R}|$ to the largest term on the rhs of each studied evolution equation was calculated. The results show that, in all three cases A, B, and C, $\mathcal{R}_N < 0.05$ for Eqs. (27) and (29) [or $\mathcal{R}_N < 0.2$ for Eq. (30)], provided that $c \in (0.1,\ 0.9)$ and $t/\tau_t^* > 0.05$. Nonsurprisingly, the relative large residual, i.e., $0.05 < \mathcal{R}_N < 0.2$ for Eq. (30), occurs mostly at sporadic values of $\hat{c}$ for $0.5 < t/\tau_t^* < 2$.

The observed match between the lhs and rhs terms shows that Eqs. (27), (29), and (30) derived in this paper can be analyzed using DNS data obtained from highly turbulent reacting waves and, in particular, from wave C associated with highly complicated instantaneous reaction zone and eventual appearance of a number of zero-gradient points where $|\nabla c| = 0$.

B. Comparison of differently weighted surface averages

To stress that (i) the difference between unweighted and area-weighted surface-averaged values of $|\nabla c|$ can be large and, therefore, (ii) a method used to evaluate surface-averaged

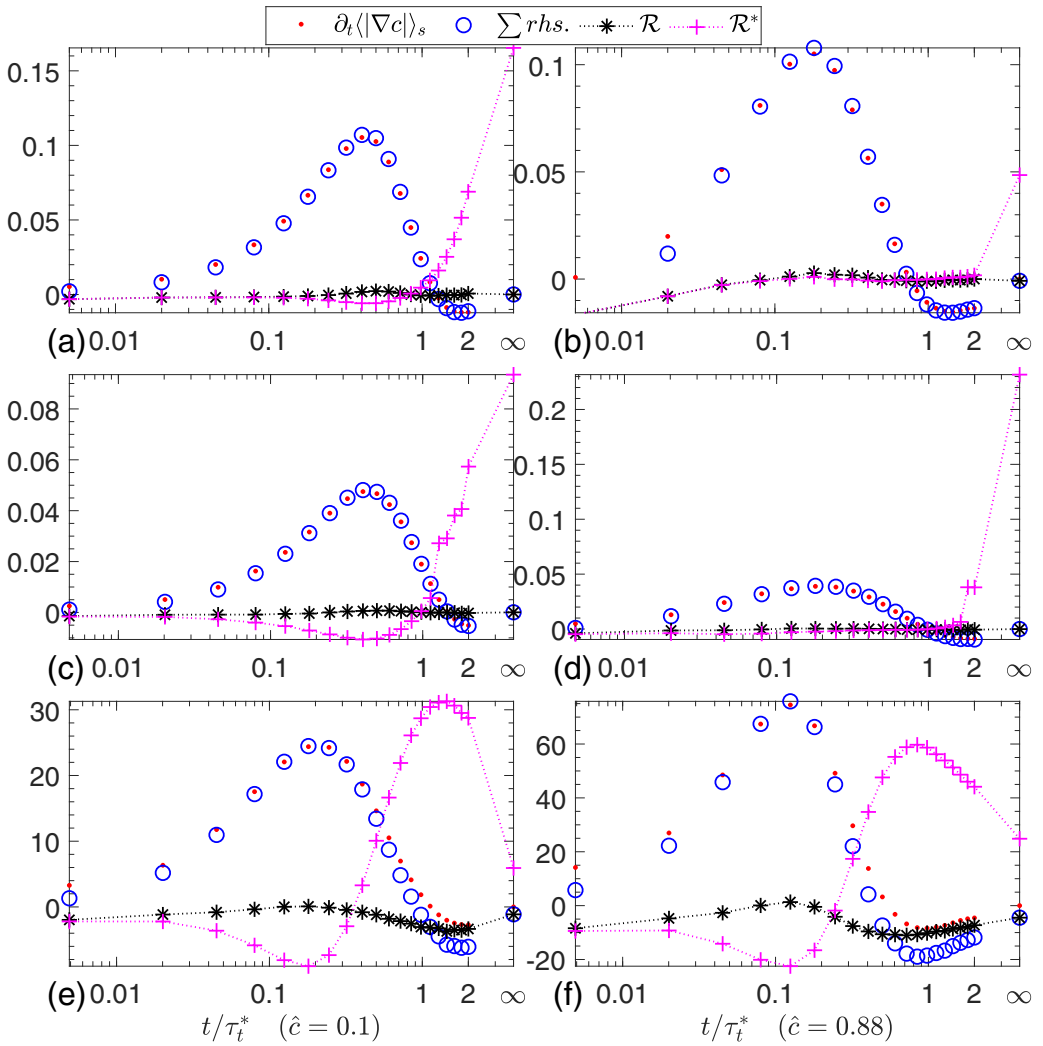

FIG. 4. Comparison of the lhs and the rhs of Eq. (27), as well as residuals $\mathcal{R} = \sum \text{rhs} - \text{lhs}$. Tweaked residuals $\mathcal{R}^*$ are computed by substituting all the area-weighted surface-averaged terms $\langle\cdot\rangle_s|_{\hat{c},t}$ on the rhs of Eq. (27) with the counterpart unweighted surface-averaged terms $\langle\cdot\rangle_v|_{\hat{c},t}$. Fine-grained results obtained for $\hat{c} = 0.1$ and $\hat{c} = 0.88$ are plotted in the left and right columns, respectively. Results computed in cases A, B, and C are reported in the up, middle, and bottom rows, respectively. All terms are normalized with S_L/δ_F^2, time is normalized with $\tau_F^* = \tau_F$ in cases A and B, or $\tau_F^* = \tau_F/22.5$ in case C.

quantities should always be discussed appropriately, tweaked residual terms $\mathcal{R}^*$ were evaluated by substituting all area-weighted terms with the counterpart unweighted terms on the rhs of Eq. (27) and vice versa on the rhs of Eq. (29). Such tweaked residual terms are plotted in magenta pluses in Figs. 4, 5, 6, and 7. In each figure, magnitudes of $\mathcal{R}^*$ are large, thus, showing importance of taking the appropriate average.

As noted earlier, the differences in the unweighted and area-weighted surface-averaged values of the quantity ϕ are caused by variations of $|\nabla c|$ along the considered isosurface, which is highly wrinkled by turbulent eddies at large u'/S_L. Since such wrinkles are less pronounced during an earlier stage of a reaction-wave development, the differences (e.g., the magnitudes of $\mathcal{R}^*$) are lower at lower t/τ_t^*. At $t \to 0$, $\mathcal{R}^* \approx \mathcal{R}$ because the two different surface averages are identical for the undisturbed laminar 1D planar wave at $t = 0$.

C. Fully developed relations

As discussed in Sec. II E, for a fully developed wave at t_∞, the evolution equations (27), (29), and (30) reduce to Eqs. (32), (33), and (34), respectively. In the constant-density case, the latter equations can further be simplified by removing terms containing the velocity divergence $\nabla \cdot \boldsymbol{u}$. These three fully developed relations are numerically examined in the right-column subfigures in Figs. 5, 7, and 9, respectively

More specifically, Figs. 5(c), 5(f), and 5(i) report the rhs terms in Eq. (27) and show that (i) $\langle\mathcal{K}\rangle_s|_{t_\infty,\hat{c}}$ plotted in green triangles vanishes and (ii) $\langle|\nabla c|\nabla\cdot(S_d\boldsymbol{n})\rangle_s|_{t_\infty,\hat{c}}$ plotted in black pentagons is a negative mirror of term $2\langle|\nabla c|\mathcal{K}\rangle_s|_{t_\infty,\hat{c}}$ (see blue squares) for all $\hat{c} \in (0, 1)$ in line with Eq. (32). Similarly, Figs. 7(c), 7(f), and 7(i) show that the rhs terms in Eq. (29) vanish (see black pentagons and blue squares). Furthermore, Figs. 9(c), 9(f), and 9(i) show that (i) $\langle S_d\rangle_s\langle\mathcal{K}\rangle_s|_{t_\infty,\hat{c}}$ plotted in magenta left pointing triangles vanishes on the rhs

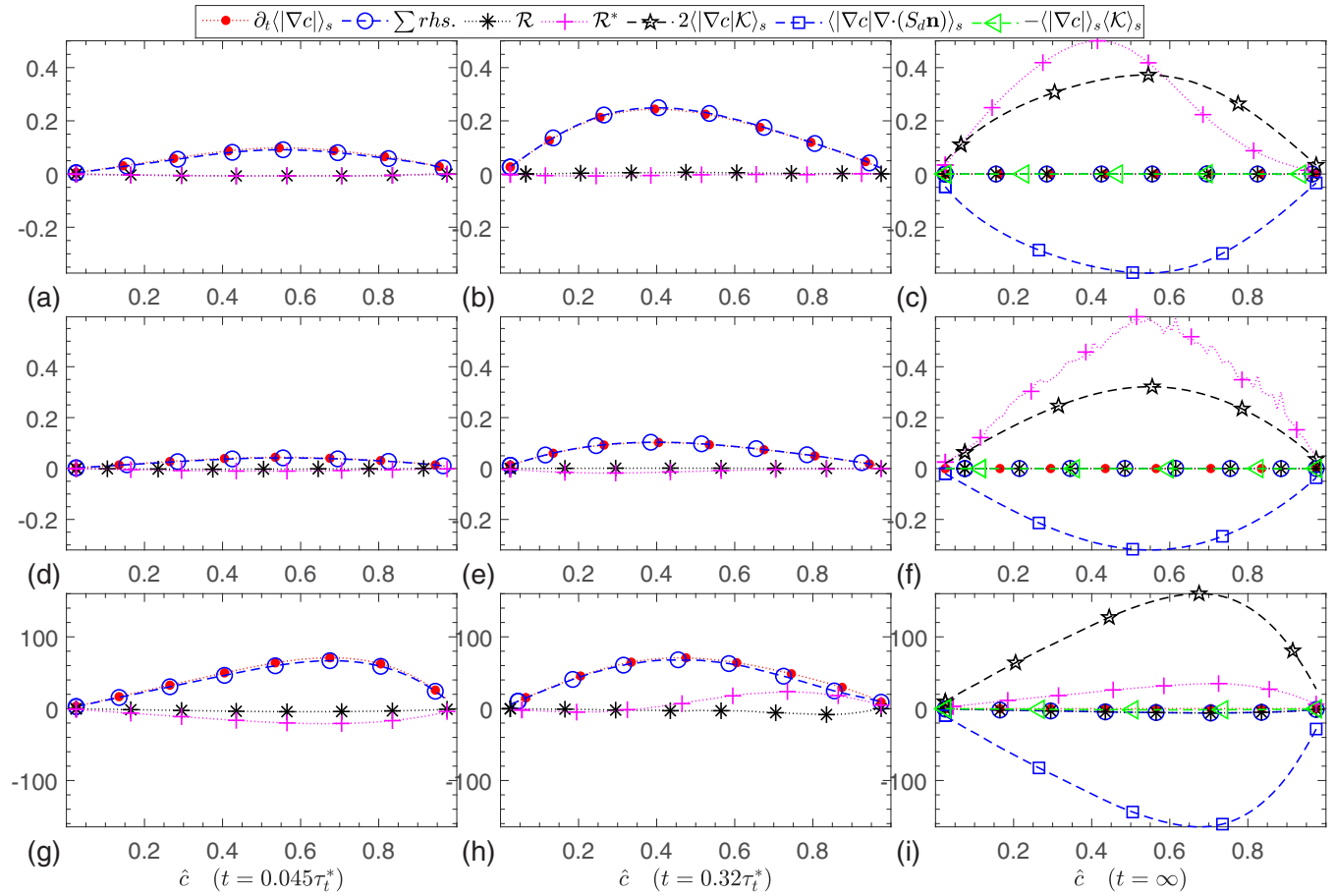

FIG. 5. Dependencies of the lhs, the rhs, and various terms on the rhs of Eq. (27) on the value of $\hat{c}$ that results are conditioned to. Black stars show residuals $\mathcal{R} = \sum \text{rhs} - \text{lhs}$. Tweaked residuals $\mathcal{R}^*$ are computed by substituting all the area-weighted surface-averaged terms $\langle\cdot\rangle_s|_{\hat{c},t}$ on the rhs of Eq. (27) with the counterpart unweighted surface-averaged terms $\langle\cdot\rangle_v|_{\hat{c},t}$. Results computed at $t = 0.045\tau_F^*$ and $t = 0.32\tau_F^*$ are plotted in the left and middle columns, respectively, with $\tau_F^* = \tau_F$ in cases A and B or $\tau_F^* = \tau_F/22.5$ in case C. Results obtained from the fully developed waves are reported in the right column. Results computed in cases A, B, and C are shown in the up, middle, and bottom rows, respectively. All terms are normalized with S_L/δ_F^2.

of Eq. (30) and (ii) the remaining terms cancel each other, with their sum being close to zero, in line with Eq. (34).

Figures 9(c), 9(f), and 9(i) show that, at various $\hat{c}$, numerically evaluated magnitudes of five terms associated with the fully developed Eq. (30), i.e., lhs, $\sum$rhs, $\mathcal{R} = \sum \text{rhs} - \text{lhs}$, $-\mathcal{D}\langle\boldsymbol{n}\cdot\nabla^2\boldsymbol{u}\rangle_s|_{\hat{c},t_\infty}$, and $\langle S_d\rangle_s\langle\mathcal{K}\rangle_s$, are much less than the magnitudes of four other terms. Note that the term $\langle S_d\nabla\cdot\boldsymbol{u}\rangle_s$ is not plotted because it vanishes in the simulated constant-density cases. Therefore, terms $-\langle S_d\nabla\cdot(S_d\boldsymbol{n})\rangle_s|_{\hat{c},t_\infty}$ (see green right-pointing triangles), $\mathcal{D}\langle\boldsymbol{n}\cdot\nabla^2(S_d\boldsymbol{n})\rangle_s|_{\hat{c},t_\infty}$ (see stars), $-2\mathcal{D}\langle\nabla\nabla c:\nabla\boldsymbol{u}/|\nabla c|\rangle_s|_{\hat{c},t_\infty}$ (see pentagons), and $2\mathcal{D}\langle\nabla\nabla c:\nabla(S_d\boldsymbol{n})/|\nabla c|\rangle_s|_{\hat{c},t_\infty}$ (see pluses) dominate in the considered equation in the studied cases.

D. Thinning or broadening of reaction waves?

Figures 4 and 6 show the same trend for evolutions of the lhs terms $\frac{\partial}{\partial t}\Psi$ for $\Psi = \langle|\nabla c|\rangle_s$ and $\Psi = \ln\langle|\nabla c|\rangle_v$), respectively. Initially, the lhs grows from zero, then reaches a positive peak, then, drops to negative values, and finally relaxes toward zero in the fully developed state. This observation indicates, in particular, that the local reaction-wave thickness decreases (the conditioned gradient of c increases) during an early stage of the wave evolution in a turbulent flow. Subsequently, the trend reverses and wave broadening is observed. Such a dynamic process can quantitatively be studied by examining the rhs terms in Eqs. (27) and (29), but this will be the subject of a followup paper [73]. Here, we restrict ourselves to a brief qualitative explanation of the emphasized trend by considering Eq. (29).

In a constant-density flow, $\nabla\cdot\boldsymbol{u} = 0$ and the early wave thinning is primely attributed to a quick increase in the positive stretch-rate term $\langle\mathcal{K}\rangle_s$, in line with the classical theory on stretching material surfaces by turbulence [72]. The later wave broadening is associated with the negative term $\langle\nabla\cdot(S_d\boldsymbol{n})\rangle_v$, whose magnitude becomes significant and overwhelms $\langle\mathcal{K}\rangle_s$ after a short initial stage.

Thus, the reported results indicate that not only the method of averaging, but also the evolution stage should be properly taken into account in studies that aim at clarifying inconsistency between available data on the local flame thickness in a turbulent flow.

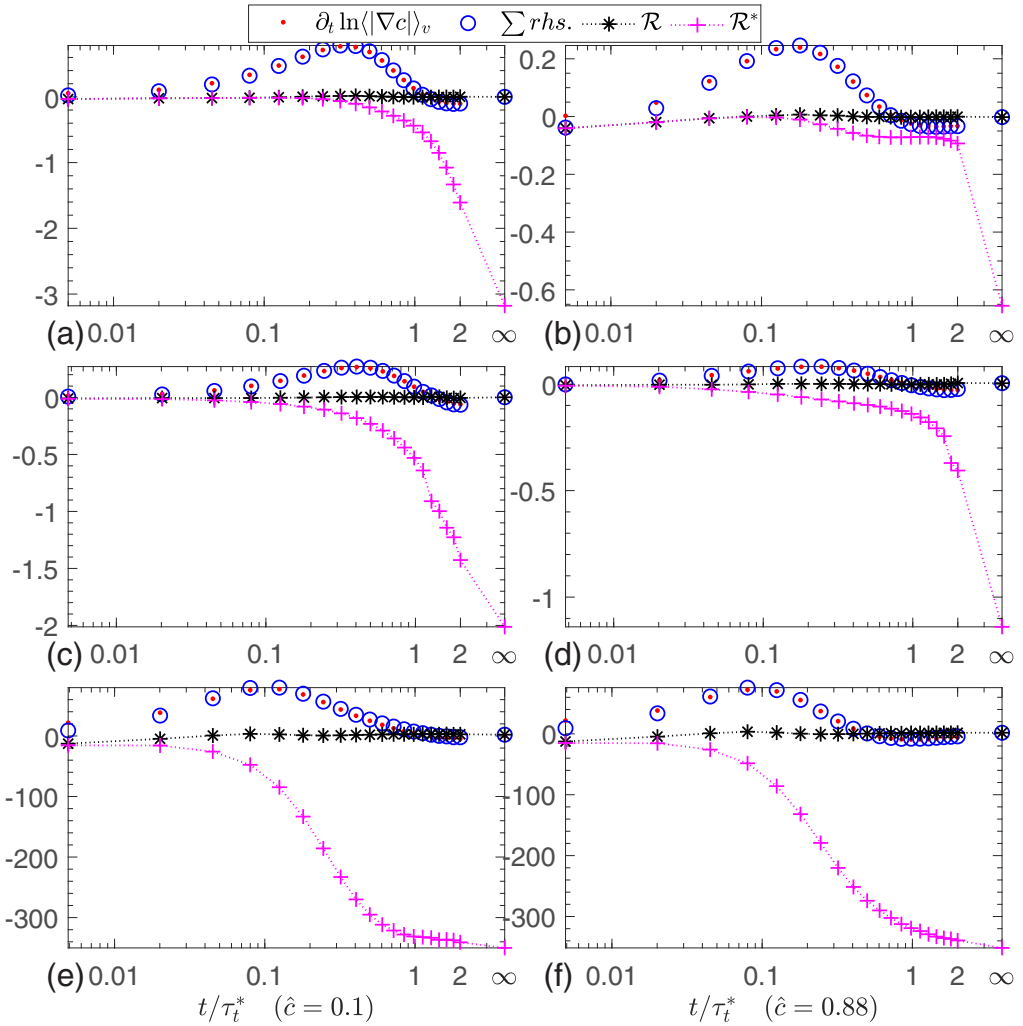

FIG. 6. Evolution of normalized terms in Eq. (29) (see caption to Fig. 4 for further details).

V. CONCLUSIONS

Two different methods for evaluating surface-averaged quantities in turbulent reacting flows, i.e., taking the area-weighted surface average $\langle\phi\rangle_s|_{\hat{c},t}$ defined by Eq. (2) and unweighted surface average $\langle\phi\rangle_v|_{\hat{c},t}$ defined by Eq. (3), were studied both analytically and numerically. Analytical relations between $\langle\phi\rangle_s|_{\hat{c},t}$ and $\langle\phi\rangle_v|_{\hat{c},t}$ were obtained and the difference between them was emphasized.

A general approach to derive evolution equations for bulk area-weighted surface-averaged quantities was developed and new evolution equations, i.e., Eqs. (27) and (29) for the area-weighted $\langle|\nabla c|\rangle_s(t)$ and unweighted $\langle|\nabla c|\rangle_v(t)$, respectively, and Eq. (30) for the area-weighted displacement speed $\langle S_d\rangle_s(t)$, were obtained using the developed approach. To obtain the $\langle S_d\rangle_s$-evolution equation, a new transport equation for $S_d(\boldsymbol{x},t)$ was also derived by invoking two additional simplifications ($\rho\mathcal{D}=$ const and the reaction rate is constant on any isosurface of the reaction progress variable c). In the case of fully developed turbulent reaction wave, the three derived evolution equations reduce to three constraints given by Eqs. (32), (33), and (34), respectively.

Analysis of DNS data computed in the case of a dynamically passive (constant-density) single reaction wave has shown that each term in the aforementioned evolution equations can be evaluated with a sufficiently high precision even in the highly turbulent case C (the Karlovitz number Ka = 390 and the Damköhler number Da = 0.02) in spite of eventual appearance of zero-gradient points in this case.

Analysis of the DNS data has also shown that artificial substitution of the area-weighted surface-averaged terms with their unweighted counterparts and vice versa results in strongly increasing residuals of the evolution equations for $\langle|\nabla c|\rangle_s$ and $\langle|\nabla c|\rangle_v$, thus, further emphasizing importance of the use of the properly defined surface-averaged quantities.

It is worth stressing that the three derived evolution equations are not limited to the constant-density case addressed in the present DNS for simplicity. Accordingly, the developed approach will be applied to variable-density complex-chemistry DNS data obtained from premixed turbulent flames [91–93] in subsequent papers.

Furthermore, this study sheds a light on the paradox of local flame thinning and broadening, which is widely discussed in the turbulent combustion literature. In particular, the present analytical and numerical results suggest that the use of

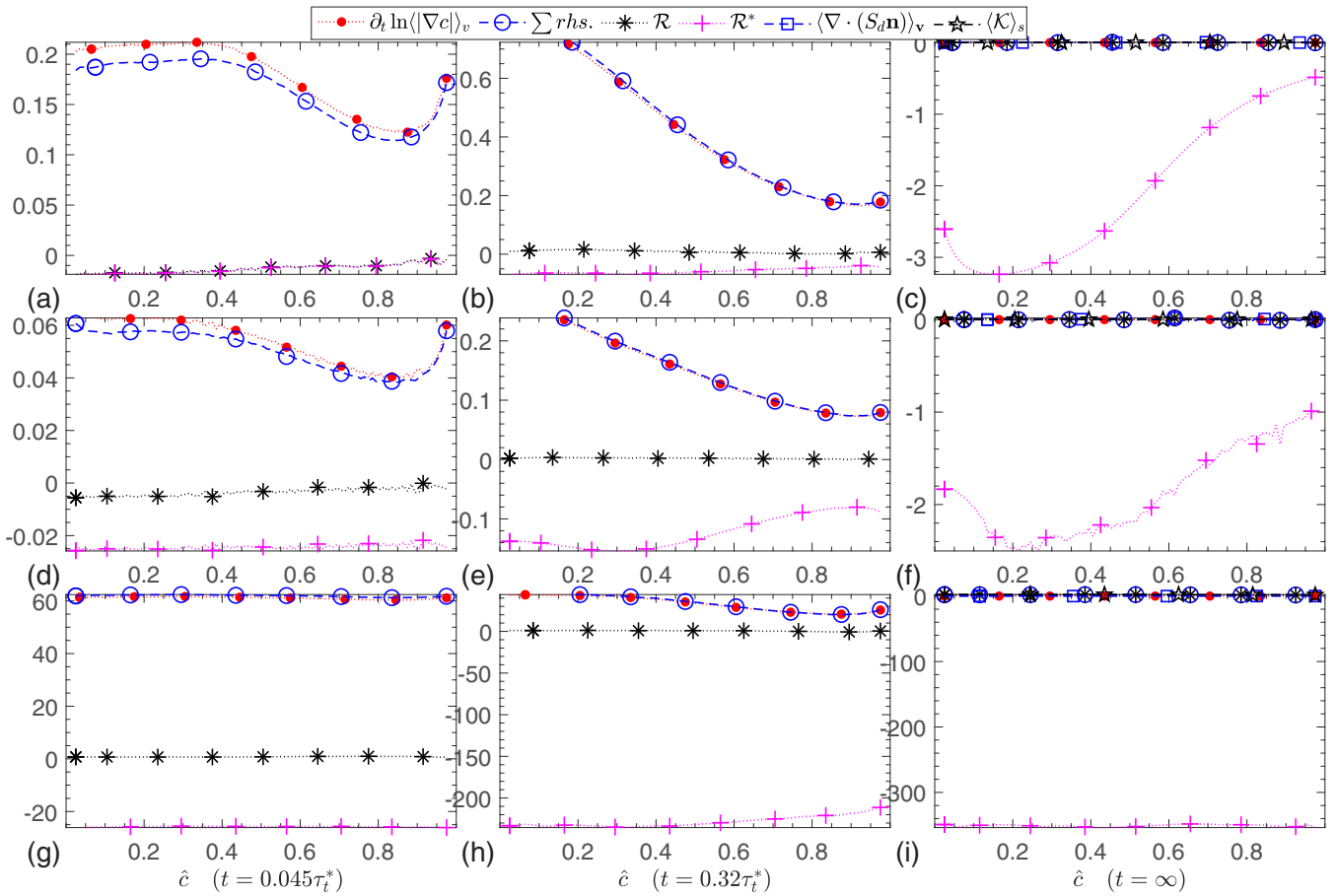

FIG. 7. $\hat{c}$ profiles of normalized terms in Eq. (29) (see caption to Fig. 5 for further details).

differently defined surface-averaged quantities and the neglect of transient effects can contribute to inconsistency between the reported data on the influence of turbulence on the local flame thickness.

Finally, the general evolution equation (25) derived in this paper can generate a family of new equations for various surface-averaged quantities, e.g., quantities that characterize the local isosurface curvature. Such equations will be addressed in future work.

ACKNOWLEDGMENTS

R.Y. gratefully acknowledges the financial support by the Swedish Research Council (VR 621-2014-5425) and thanks T. Nillsson for constructive discussions. A.L. gratefully acknowledges the financial support by CERC. The simulations were performed using the computer facilities provided by the Swedish National Infrastructure for Computing (SNIC) at Beskow-PDC Center.

APPENDIX A: EQUATION FOR THE SECOND MOMENT OF SURFACE-CONDITIONED FLUCTUATIONS

Substitution of ϕ with ϕ^2 in Eq. (11) results in $\widehat{A\langle\phi^2\rangle}_s = \widehat{\int\int_S \phi^2\, ds}$. Differentiation of this equality with respect to time yields the following evolution equation:

$$\frac{\partial\langle\phi^2\rangle_s}{\partial t} = 2\left\langle\phi\frac{\partial^*}{\partial^* t}\phi\right\rangle_s + \langle\phi^2\mathcal{K}\rangle_s - \langle\phi^2\rangle_s\langle\mathcal{K}\rangle_s. \tag{A1}$$

Multiplying Eq. (25) with $2\langle\phi\rangle_s$ and subtracting the obtained equation from Eq. (A1), we arrive at the evolution equation

$$\frac{\partial\langle\phi''^2\rangle_s}{\partial t} = 2\left\langle\phi\frac{\partial^*}{\partial^* t}\phi\right\rangle_s - 2\langle\phi\rangle_s\left\langle\frac{\partial^*}{\partial^* t}\phi\right\rangle_s + \langle\phi^2\mathcal{K}\rangle_s - 2\langle\phi\rangle_s\langle\phi\mathcal{K}\rangle_s + (\langle\phi''^2\rangle_s - \langle\phi\rangle_s^2)\langle\mathcal{K}\rangle_s \tag{A2}$$

for the second moment

$$\langle\phi''^2\rangle_s = \langle\phi^2\rangle_s - \langle\phi\rangle_s^2. \tag{A3}$$

Here, contrary to Eq. (8), fluctuations are defined within the area-weighted framework, i.e., $\phi'' \equiv \phi - \langle\phi\rangle_s$.

APPENDIX B: ISOSURFACE-FOLLOWING EQUATION FOR $|\nabla c|$

Application of operator $\partial/\partial x_i$ to Eq. (19) followed by multiplication of obtained equation with $\partial c/\partial x_i$ yields

$$\frac{\partial c}{\partial x_i}\frac{\partial^2 c}{\partial t\,\partial x_i} + (u_j - S_d n_j)\frac{\partial c}{\partial x_i}\frac{\partial^2 c}{\partial x_i\partial x_j} + \left(\frac{\partial u_j}{\partial x_i} - S_d\frac{\partial n_j}{\partial x_i} - n_j\frac{\partial S_d}{\partial x_i}\right)\frac{\partial c}{\partial x_j}\frac{\partial c}{\partial x_i} = 0, \tag{B1}$$

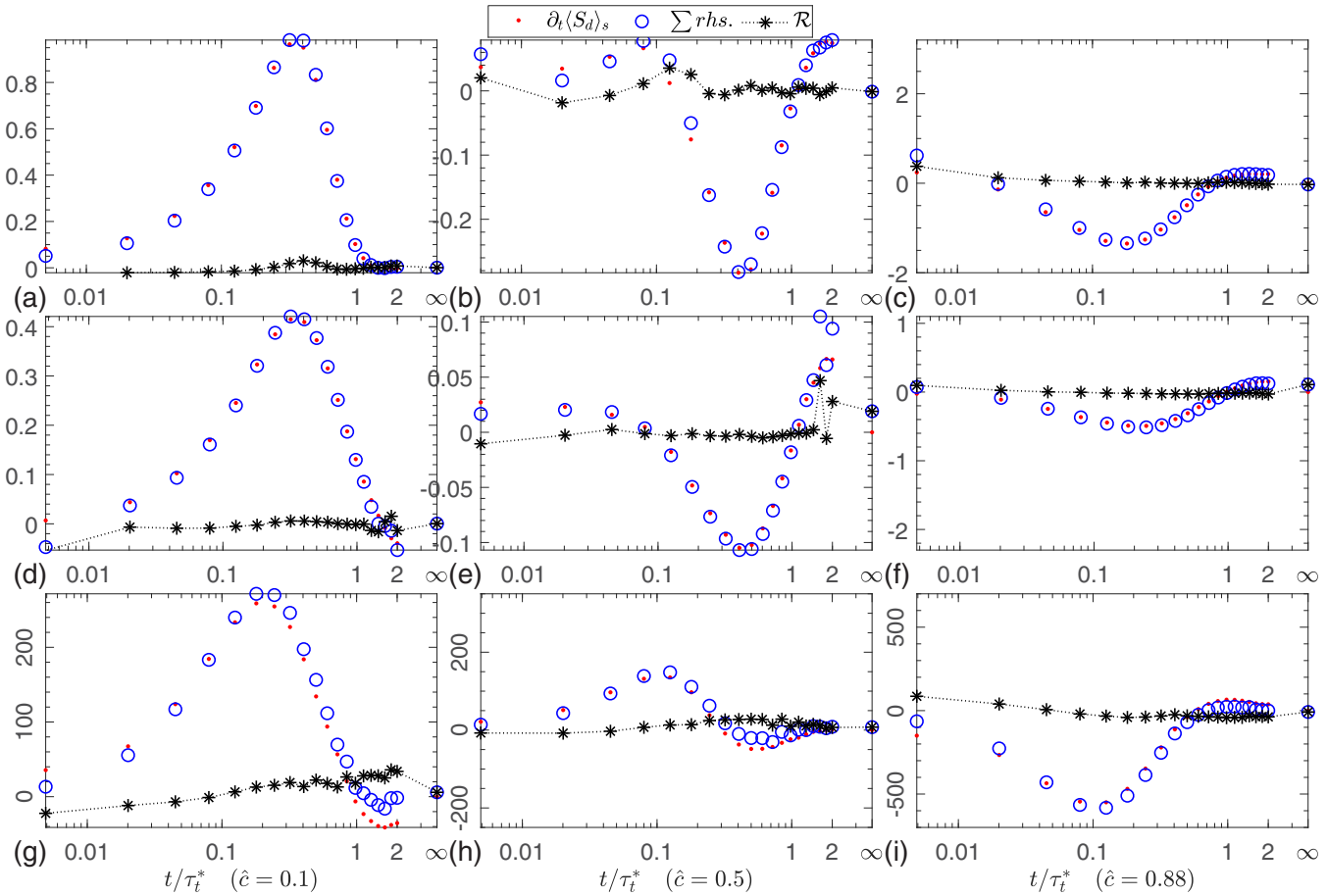

FIG. 8. Evolution of normalized terms in Eq. (30) (see caption to Fig. 4 for further details).

where the summation convention applies to repeated indices. Multiplication of this equation with $1/|\nabla c|$, differentiation of $|\nabla c|$ with respect to time and spatial coordinates, and the use of $\partial c/\partial x_i = n_i|\nabla c|$ result in

$$\frac{\partial}{\partial t}|\nabla c| + (u_j - S_d n_j)\frac{\partial}{\partial x_j}|\nabla c| + \left(\frac{\partial u_j}{\partial x_i} - S_d\frac{\partial n_j}{\partial x_i} - n_j\frac{\partial S_d}{\partial x_i}\right)n_j n_i|\nabla c| = 0. \quad \text{(B2)}$$

Finally, since $n_j n_j = 1$ and $n_j(\partial n_j/\partial x_i) = 0$, we arrive at

$$\frac{\partial^*}{\partial^* t}\ln|\nabla c| = \frac{1}{|\nabla c|}\frac{\partial^*}{\partial^* t}|\nabla c| = -a_n + \boldsymbol{n}\cdot\nabla S_d \quad \text{(B3)}$$

$$= \mathcal{K} - \nabla\cdot\boldsymbol{u} + \nabla\cdot(S_d\boldsymbol{n}) \quad \text{(B4)}$$

$$= \mathcal{K} - \nabla\cdot\boldsymbol{u}^* \quad \text{(B5)}$$

using Eq. (18).

APPENDIX C: ISOSURFACE-FOLLOWING TRANSPORT EQUATION FOR DISPLACEMENT SPEED

Let us (i) rewrite Eq. (16) as

$$S_d|\nabla c| = \frac{1}{\rho}\nabla\cdot(\rho\mathcal{D}\nabla c) + \mathbb{W}, \quad \text{(C1)}$$

(ii) assume that the diffusivity $\rho\mathcal{D}$ is constant and the reaction rate depends solely on c, and (iii) take the isosurface-following derivative of both sides of the above equation. Then, the following equation holds:

$$\frac{\partial^*}{\partial^* t}(S_d|\nabla c|) = \mathcal{D}\frac{\partial^*}{\partial^* t}(\nabla^2 c) + \frac{\partial^*}{\partial^* t}\mathbb{W}, \quad \text{(C2)}$$

with the last term on its rhs vanishing due to the assumption of $\mathbb{W} = \mathbb{W}(c)$ and Eq. (20). Consequently,

$$\frac{\partial^*}{\partial^* t}S_d = -\frac{S_d}{|\nabla c|}\frac{\partial^*}{\partial^* t}|\nabla c| + \frac{\mathcal{D}}{|\nabla c|}\frac{\partial^*}{\partial^* t}(\nabla^2 c). \quad \text{(C3)}$$

Substituting $\boldsymbol{a} = \boldsymbol{u}^*$ and $\boldsymbol{b} = \nabla c$ into the identity

$$a_i\frac{\partial^2 b_i}{\partial x_j\partial x_j} = \frac{\partial^2(a_i b_i)}{\partial x_j\partial x_j} - b_i\frac{\partial^2 a_i}{\partial x_j\partial x_j} - 2\frac{\partial a_i}{\partial x_j}\frac{\partial b_i}{\partial x_j} \quad \text{(C4)}$$

and taking into account Eq. (20), the second term on the rhs of Eq. (C3) can be transformed to

$$\frac{\partial^*}{\partial^* t}(\nabla^2 c) = \frac{\partial}{\partial t}\frac{\partial^2 c}{\partial x_j\partial x_j} + u_i^*\frac{\partial}{\partial x_i}\frac{\partial^2 c}{\partial x_j\partial x_j} \quad \text{(C5)}$$

$$= \frac{\partial^2}{\partial x_j\partial x_j}\left(\frac{\partial}{\partial t}c + u_i^*\frac{\partial c}{\partial x_i}\right) - \frac{\partial c}{\partial x_i}\frac{\partial^2 u_i^*}{\partial x_j\partial x_j} - 2\frac{\partial^2 c}{\partial x_i\partial x_j}\frac{\partial u_i^*}{\partial x_j} \quad \text{(C6)}$$

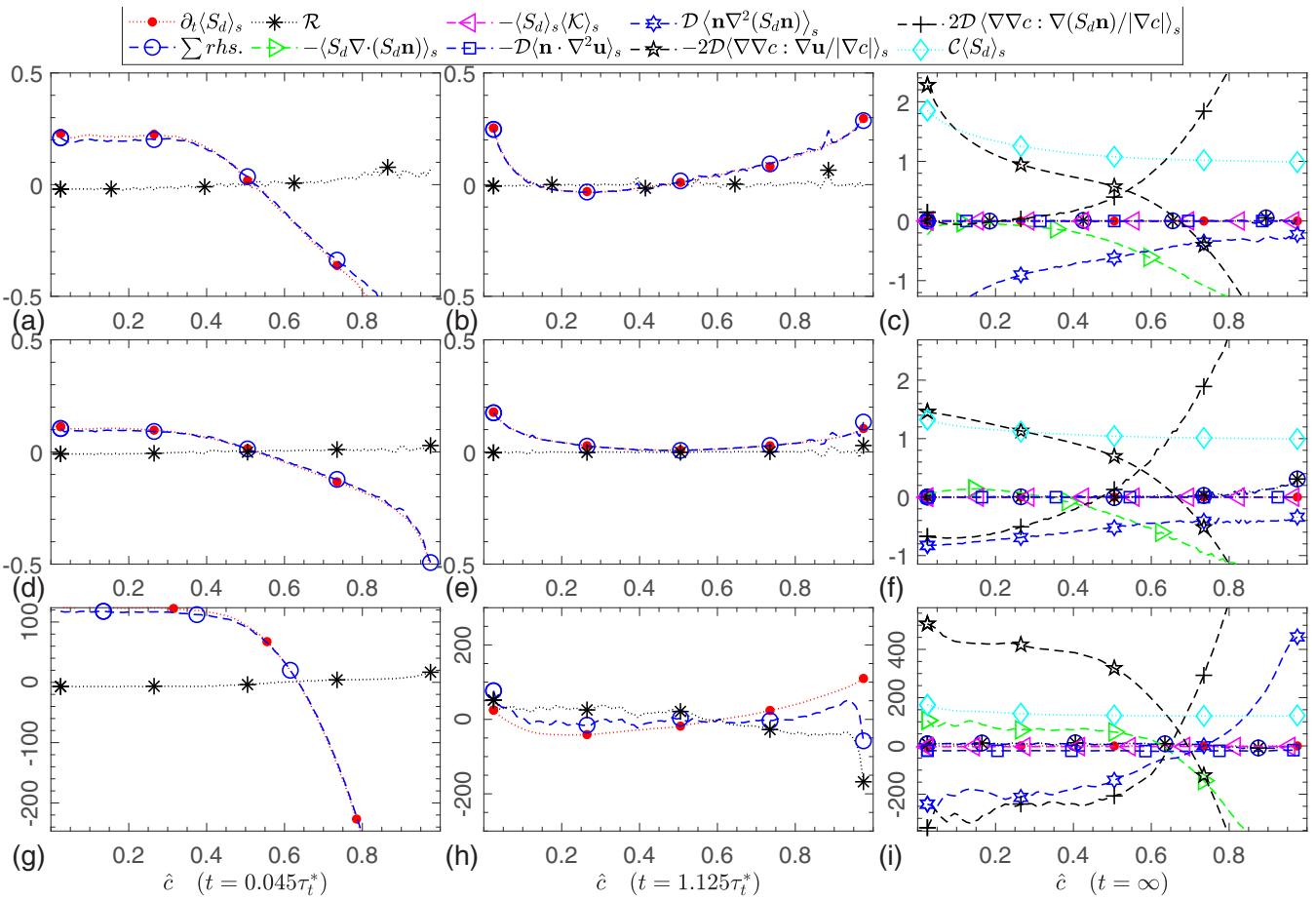

FIG. 9. $\hat{c}$ profiles of terms in Eq. (30), appropriately normalized based on S_L and δ_F and plotted similarity as in Fig. 5. $\mathcal{C}=1$ in cases A and B (up and middle row) or $\mathcal{C}=100$ in case C (bottom row). All 10 terms listed in legends are shown in the right column, but 5 terms are difficult to distinguish because their magnitudes are low.

$$= -\frac{\partial c}{\partial x_i}\frac{\partial^2 u_i^*}{\partial x_j^2} - 2\frac{\partial^2 c}{\partial x_i \partial x_j}\frac{\partial u_i^*}{\partial x_j} \tag{C7}$$

$$= -\nabla c\cdot\nabla^2\boldsymbol{u}^* - 2\nabla\nabla c:\nabla\boldsymbol{u}^*. \tag{C8}$$

Subsequently, substitution of Eqs. (B5) and (C8) with $\boldsymbol{u}^* \equiv \boldsymbol{u} - S_d\boldsymbol{n}$ into the first and second terms on the rhs of Eq. (C3), respectively, yields the following transport equation for the displacement speed:

$$\begin{aligned}\frac{\partial^*}{\partial^* t}S_d = &-S_d[\mathcal{K} + \nabla\cdot(S_d\boldsymbol{n}) - \nabla\cdot\boldsymbol{u}] \\ &- \mathcal{D}\boldsymbol{n}\cdot\nabla^2\boldsymbol{u} + \mathcal{D}\boldsymbol{n}\cdot\nabla^2(S_d\boldsymbol{n}) \\ &- \frac{2\mathcal{D}}{|\nabla c|}\nabla\nabla c:\nabla\boldsymbol{u} + \frac{2\mathcal{D}}{|\nabla c|}\nabla\nabla c:\nabla(S_d\boldsymbol{n}).\end{aligned} \tag{C9}$$

The third term on the rhs of Eq. (C9) can be decomposed as follows:

$$\mathcal{D}\boldsymbol{n}\cdot\nabla^2(S_d\boldsymbol{n}) = \mathcal{D}\nabla^2 S_d + \mathcal{D}S_d\boldsymbol{n}\cdot\nabla^2\boldsymbol{n}. \tag{C10}$$

Moreover, by applying Laplacian ∇^2 to the identity of $n_i n_i = 1$, we obtain

$$\boldsymbol{n}\cdot\nabla^2\boldsymbol{n} \equiv n_i\frac{\partial^2 n_i}{\partial x_j\partial x_j} = -\frac{\partial n_i}{\partial x_j}\frac{\partial n_i}{\partial x_j} = -\nabla\boldsymbol{n}:\nabla\boldsymbol{n}. \tag{C11}$$

Then, the last term on the rhs of Eq. (C9) reads as

$$\begin{aligned}\frac{\nabla\nabla c:\nabla(S_d\boldsymbol{n})}{|\nabla c|} &= \frac{1}{|\nabla c|}\frac{\partial^2 c}{\partial x_i\partial x_j}\left(n_i\frac{\partial S_d}{\partial x_j} + S_d\frac{\partial n_i}{\partial x_j}\right) \\ &= \frac{\partial S_d}{\partial x_j}\frac{1}{|\nabla c|^2}\frac{\partial^2 c}{\partial x_i\partial x_j}\frac{\partial c}{\partial x_i} + S_d\frac{1}{|\nabla c|}\frac{\partial^2 c}{\partial x_i\partial x_j}\frac{\partial n_i}{\partial x_j} \\ &= \frac{\partial S_d}{\partial x_j}\frac{1}{2|\nabla c|^2}\frac{\partial}{\partial x_j}(|\nabla c|^2) \\ &\quad + S_d\frac{1}{|\nabla c|}\frac{\partial(n_i|\nabla c|)}{\partial x_j}\frac{\partial n_i}{\partial x_j} \\ &= \frac{\partial S_d}{\partial x_j}\frac{1}{|\nabla c|}\frac{\partial}{\partial x_j}|\nabla c| \\ &\quad + S_d\left(\frac{\partial n_i}{\partial x_j}\frac{\partial n_i}{\partial x_j} + \frac{1}{2|\nabla c|}\frac{\partial(|\nabla c|)}{\partial x_j}\frac{\partial(n_i n_i)}{\partial x_j}\right) \\ &= \nabla S_d\cdot\nabla(\ln|\nabla c|) - S_d\boldsymbol{n}\cdot\nabla^2\boldsymbol{n},\end{aligned} \tag{C12}$$

where factor $2\mathcal{D}$ is skipped for brevity. Finally, substitution of Eqs. (C10) and (C12) into Eq. (C9) yields

$$\frac{\partial^*}{\partial^* t}S_d = \underbrace{-S_d[\mathcal{K} + \boldsymbol{\nabla}\cdot(S_d\boldsymbol{n}) - \boldsymbol{\nabla}\cdot\boldsymbol{u}]}_{\text{I}} \underbrace{-\mathcal{D}\left(\boldsymbol{n}\cdot\nabla^2\boldsymbol{u} + \frac{2\boldsymbol{\nabla}\boldsymbol{\nabla}c:\boldsymbol{\nabla}\boldsymbol{u}}{|\boldsymbol{\nabla}c|}\right)}_{\text{II}} + \underbrace{\mathcal{D}\nabla^2 S_d}_{\text{III}} + \underbrace{2\mathcal{D}\boldsymbol{\nabla}S_d\cdot\boldsymbol{\nabla}(\ln|\boldsymbol{\nabla}c|)}_{\text{IV}} \underbrace{-\mathcal{D}S_d\boldsymbol{n}\cdot\nabla^2\boldsymbol{n}}_{\text{V}}. \tag{C13}$$

On the rhs, the five terms are associated with contributions due to (I) the rate of change of $|\boldsymbol{\nabla}c|$ conditioned to an isosurface, i.e., $\partial^*\ln|\boldsymbol{\nabla}c|/\partial^* t$; (II) interaction between turbulent flow $\boldsymbol{u}$ and reactive scalar field c; (III) "molecular transport" of S_d; (IV) a modified convection vector $2\vec{\mathbb{S}}_d^n\cdot\boldsymbol{\nabla}S_d$, where $\vec{\mathbb{S}}_d^n \equiv \mathcal{D}\boldsymbol{\nabla}(\ln|\boldsymbol{\nabla}c|)$ is related to the normal-diffusion contribution $S_d^n \equiv \frac{\boldsymbol{n}}{|\boldsymbol{\nabla}c|}\cdot\boldsymbol{\nabla}(\mathcal{D}|\boldsymbol{\nabla}c|)$ to the displacement speed, i.e. $S_d^n = \boldsymbol{n}\cdot\vec{\mathbb{S}}_d^n$; (V) spatial nonuniformities of $\boldsymbol{n}$ in the normal direction.

APPENDIX D: SOME NUMERICAL ASPECTS

1. Transient simulations in cases A and B

In the two frozen-velocity cases A and B, the transient simulations are performed in the way already discussed above in case C, but there are some differences. First, the duration of transient sampling is changed from $2\tau_t^0$ to $2\tau_F$. Second, at each reset instant, a random number $-1/4 < r^* < 1/4$ is added to perturb the position of the embedded wave, i.e., $x_m/\Lambda_x = (m - 0.5 + r^*)/\mathcal{M}$. Without use of such a random number, the effective total number M_t^{eff} of realizations used for sampling transient statistics would be equal to $\mathcal{M}$ instead of $\mathcal{M}\times J$ because the evolution of each transient wave c_m^t in a frozen flow would be identical after each reset event. Even with the random perturbations, the effective total number M_t^{eff} is limited by the scales of frozen flow field, thus impeding increasing realization number by increasing the number J of the reset events.

The above limitations also affect the fully developed statistics sampled using c^s, but the effect magnitude is expected to be less. When a c^s wave continuously cycles through the periodic frozen turbulence field, the evolution of wave can be partially random. By analyzing the computed data, it has been confirmed that the c^s fields appear differently during different evolution cycles.

2. Calculation of surface-averaged quantities

The fine-grained, area-weighted surface-averaged $\langle\phi\rangle_s|_{\hat{c},t}$ are computed using two different approaches. One method is based on Eq. (11), which does not involve Dirac delta function. Accordingly, Eq. (11) appears to provide a direct method for numerically calculating the area-weighted surface averages. In an applied CFD code, which deals typically with a discrete grid, the fields of $c_{(i)}(\boldsymbol{x},t)$ and $\phi_{(i)}(\boldsymbol{x},t)$ are often represented using an isosurface extraction algorithm such as the marching cube method [94]. Accordingly, the implicit surface $S_{(i)}$ of $c_{(i)}(\boldsymbol{x},t) = \hat{c}$ is extracted as a collection of triangulated surface elements. Subsequently, the area-weighted integration in Eq. (11) is approximated by summing the product of each triangular area with the value of ϕ interpolated to the triangle center. When applying such an algorithm, the accuracy of the discrete representation of the isosurface $S_{(i)}$ is limited by the accuracy of the adopted isosurface-extraction method. The latter accuracy can be improved by interpolating c and ϕ with a higher order accuracy from the original discrete grid to a new, much finer grid, followed by extraction of a discrete isosurface using the latter grid. This method is straightforward, but potentially expensive. The accuracy can also be improved by increasing the number of realizations M.

Another method is based on rewriting the definitions of the area-weighted and unweighted surface-averaged quantities, given by Eqs. (2) and (3), in the following forms:

$$\langle\phi\rangle_s|_{\hat{c},t} = \lim_{\epsilon\to 0}\langle\phi\rangle_s|_{\hat{c},\epsilon,t} \tag{D1}$$

and

$$\langle\phi\rangle_v|_{\hat{c},t} = \lim_{\epsilon\to 0}\langle\phi\rangle_v|_{\hat{c},\epsilon,t}. \tag{D2}$$

Here,

$$\langle\phi\rangle_s|_{\hat{c},\epsilon,t} \equiv \frac{\overline{\phi|\boldsymbol{\nabla}c|1_{\hat{c},\epsilon}}}{\overline{|\boldsymbol{\nabla}c|1_{\hat{c},\epsilon}}} = \lim_{M\to\infty}\frac{\sum_{i=1}^M\iiint_V\phi_{(i)}|\boldsymbol{\nabla}c_{(i)}|1_{\hat{c},\epsilon}\,d\boldsymbol{x}}{\sum_{i=1}^M\iiint_V|\boldsymbol{\nabla}c_{(i)}|\,1_{\hat{c},\epsilon}\,d\boldsymbol{x}} \tag{D3}$$

and

$$\langle\phi\rangle_v|_{\hat{c},\epsilon,t} \equiv \frac{\overline{\phi 1_{\hat{c},\epsilon}}}{\overline{1_{\hat{c},\epsilon}}} = \lim_{M\to\infty}\frac{\sum_{i=1}^M\iiint_V\phi_{(i)}\cdot 1_{\hat{c},\epsilon}\,d\boldsymbol{x}}{\sum_{i=1}^M\iiint_V 1_{\hat{c},\epsilon}\,d\boldsymbol{x}}, \tag{D4}$$

respectively, the sifting function

$$1_{\hat{c},\epsilon} \equiv H(c-\hat{c}) - H(c-\hat{c}-\epsilon) \tag{D5}$$

allows us to select c within an interval of $[\hat{c},\hat{c}+\epsilon]$, $\epsilon < 1$ is a positive number, $H(c)$ is Heaviside function. Then, the quantities $\langle\phi\rangle_s|_{\hat{c},t}$ and $\langle\phi\rangle_v|_{\hat{c},t}$ may be interpreted as "fine-grained" values of ϕ, averaged over a single isosurface of $c(\boldsymbol{x},t) = \hat{c}$, whereas the quantities $\langle\phi\rangle_s|_{\hat{c},\epsilon,t}$ and $\langle\phi\rangle_v|_{\hat{c},\epsilon,t}$, defined by Eqs. (D3) and (D4), respectively, are "coarse-grained" values of ϕ, averaged over all isosurfaces of $c(\boldsymbol{x},t) = c^{\text{iso}}$ such that $c^{\text{iso}}\in[\hat{c},\hat{c}+\epsilon]$.

The spatial integration of Eq. (D3) can easily be performed by summing products of each grid cell volume with the value of $(\phi|\boldsymbol{\nabla}c|1|_{\hat{c},\epsilon})$ at the cell center. A similar method can be adopted to evaluate the fine-grained unweighted surface averages using Eqs. (D2) and (D4). It is noted, however, that, if the differences $(c-\hat{c})$ in two neighboring cells are larger than a threshold ϵ, but have opposite signs, then this simple method of numerically evaluating $\langle\phi\rangle_s$ will not sample the isosurface pieces that pass between the two cells. On the contrary, the former method based on Eq. (11) and an isosurface extraction algorithm allows us to sample such isosurface pieces. Thus, while the numerical approach based on Eqs. (D1) and (D3) is easy to implement, the alternative method has its own advantages.

Accordingly, both approaches were tested by processing $M > 20$ statistically independent fields of $(c^s, \boldsymbol{u}, p)$ in order to evaluate the fully developed values of $\langle\phi\rangle_s|_{\hat{c},t_\infty}$ for the isosurface $S_{(i)}$ of $c_{(i)}(\boldsymbol{x},t) = 0.8$. Henceforth, subscript t_∞ designates the fully developed quantity. The coarse grained $\langle\phi\rangle_s|_{\hat{c},\epsilon,t_\infty}$ was evaluated using Eq. (D3) with $\hat{c} = 0.8 - \epsilon/2$ and four values of $\epsilon = 0.01$, 0.06, 0.1, and 0.3. The obtained results (not shown) verified that the coarse-grained area-weighted surface averages of $|\nabla c|$, $1/|\nabla c|$, S_d, $\nabla\cdot\boldsymbol{n}$ did become sufficiently close to their fine-grained counterparts at $\epsilon = 0.01$ in spite of a relatively small number of processed realizations.

Since this test validated both approaches, solely the latter (simpler) method with $\epsilon = 0.01$ was subsequently used to evaluate the fine-grained area-weighted averages $\langle\phi\rangle_s|_{\hat{c},t}$ (or the unweighted averages $\langle\phi\rangle_v|_{\hat{c},t}$). To do so, the total number of realizations was set as large as $M > 1000$ (or $M > 400$, which corresponds to $\mathcal{J} > 27$ for $\mathcal{M} = 15$) in both Eqs. (D3) and (D4) when computing the fully developed averages at $t = \infty$ (or the transient averages at $0 \leqslant t \leqslant 2\tau_t^0$, respectively). The adopted simple implementation of spatial integration ($\iiint_V \ldots d\boldsymbol{x}$) by discretely sampling values on the original (not interpolation-refined) computational grid required an increase in M with decreasing ϵ in order to achieve sufficient sampling counts. Nevertheless, results obtained using the aforementioned M differ barely from results computed with $2M$ in the highly turbulent case C. Moreover, further decrease in ϵ from 0.01 to 0.005 barely changed the results, thus, also indicating that the processed number of realizations was appropriate.

Finally, it is worth stressing that the main test of the method adopted for evaluating surface-averaged quantities [including the lack of any threshold for throwing out local events characterized by abnormally large $|\phi(\boldsymbol{x},t)|$ at small distances from zero-gradient points] consists in comparison of the sums of terms on the lhs and rhs of the studied evolution equations.

3. Evaluation of various terms in the evolution equations

To evaluate all terms in these equations during simulations, all spatial derivatives in those terms are approximated using sixth order center difference and composite terms are evaluated by successively applying the sixth order approximation of derivative operator to relevant intermediate quantities evaluated at the cell center. For instance, the composite term $|\nabla c|\nabla\cdot(S_d\boldsymbol{n})$ in Eq. (27) contains terms $|\nabla c|$, S_d, $\boldsymbol{n}$, and $S_d\boldsymbol{n}$. The four quantities n_x, n_y, n_z, and $|\nabla c|$ are directly obtained by evaluating the three derivatives $\partial_x c$, $\partial_y c$, $\partial_z c$ in the cell center using the sixth order center difference. The same method is applied to computing $\nabla^2 c$ in $S_d = (\mathcal{D}\nabla^2 c + W)/|\nabla c|$. Then, term $\nabla\cdot(S_d\boldsymbol{n}) = \partial_x(S_d n_x) + \partial_y(S_d n_y) + \partial_z(S_d n_z)$ is computed by applying the sixth order center difference to the intermediate composite values of $S_d n_x$, $S_d n_y$, and $S_d n_z$, which are already obtained in the cell center.

To evaluate time derivatives of surface-averaged quantities $\Psi(t)$ on lhs's of the studied evolution equations, a sequence of transient values of Ψ is calculated at 20 sampling instants $t_i = (i^2/200)\tau_F^*$, where $i = (1,\ldots,20)$, and, then, a discrete approximation of the time derivative (i.e., the gradient function in "MATLAB") is applied to this sequence.

[1] P. D. Ronney, B. D. Haslam, and N. O. Rhys, Phys. Rev. Lett. **74**, 3804 (1995).
[2] S. Chaudhuri, F. Wu, and C. K. Law, Phys. Rev. E **88**, 033005 (2013).
[3] S. Chaudhuri, Phys. Rev. E **91**, 021001(R) (2015).
[4] R. Yu, X. S. Bai, and V. Bychkov, Phys. Rev. E **92**, 063028 (2015).
[5] C. A. Z. Towery, A. Y. Poludnenko, J. Urzay, J. O'Brien, M. Ihme, and P. E. Hamlington, Phys. Rev. E **93**, 053115 (2016).
[6] F. Creta, R. Lamioni, P. E. Lapenna, and G. Troiani, Phys. Rev. E **94**, 053102 (2016).
[7] A. Y. Poludnenko, T. A. Gardiner, and E. S. Oran, Phys. Rev. Lett. **107**, 054501 (2011).
[8] V. Akkerman, S. Chaudhuri, and C. K. Law, Phys. Rev. E **87**, 023008 (2013).
[9] V. N. Gamezo, A. M. Khokhlov, E. S. Oran, A. Y. Chtchelkanova, and R. O. Rosenberg, Science **299**, 77 (2003).
[10] V. N. Gamezo, A. M. Khokhlov, and E. S. Oran, Phys. Rev. Lett. **92**, 211102 (2004).
[11] G. Z. Damköhler, Z. Elektrochem. Angew. Phys. Chem. **46**, 601 (1940) [English translation: NACA Tech. Memo. 1112 (1947)].
[12] K. I. Shelkin, J. Tech. Phys. (USSR) **13**, 520 (1943) [English translation: NACA Tech. Memo. No. 1110 (1947)].
[13] G. V. Nivarti and R. S. Cant, Proc. Combust. Inst. **36**, 1903 (2017).
[14] V. A. Sabelnikov, R. Yu, and A. N. Lipatnikov, Int. J. Heat Mass Transfer **128**, 1201 (2019).
[15] V. A. Sabelnikov, R. Yu, and A. N. Lipatnikov, Phys. Fluids **31**, 055104 (2019).
[16] D. Veynante and L. Vervisch, Prog. Energy Combust. Sci. **28**, 193 (2002).
[17] P. Clavin, Prog. Energy Combust. Sci. **11**, 1 (1985).
[18] S. B. Pope, Int. J. Eng. Sci. **26**, 445 (1988).
[19] S. M. Candel and T. Poinsot, Combust. Sci. Technol. **70**, 1 (1990).
[20] C. Dopazo, J. Martin, and J. Hierro, Phys. Rev. E **76**, 056316 (2007).
[21] V. R. Kuznetsov and V. A. Sabelnikov, *Turbulence and Combustion* (Hemisphere, New York, 1990).
[22] A. N. Lipatnikov and J. Chomiak, Prog. Energy Combust. Sci. **31**, 1 (2005).
[23] A. Lipatnikov, *Fundamentals of Premixed Turbulent Combustion* (CRC Press, Boca Raton, FL, 2012).
[24] P. Venkateswaran, A. Marshall, J. Seitzman, and T. Lieuwen, Combust. Flame **162**, 375 (2015).
[25] W. Zhang, J. Wang, Q. Yu, W. Jin, M. Zhang, and Z. Huang, Combust. Sci. Technol. **190**, 1354 (2018).
[26] S. Yang, A. Saha, W. Liang, F. Wu, and C. K. Law, Combust. Flame **188**, 498 (2018).
[27] A. N. Lipatnikov, N. Chakraborty, and V. A. Sabelnikov, Int. J. Hydrogen Energy **43**, 21060 (2018).
[28] M. Matalon and B. J. Matkowsky, J. Fluid Mech. **124**, 239 (1982).
[29] C. Dopazo, Phys. Fluids **11**, 2952 (1999).

[30] N. Chakraborty and R. S. Cant, Phys. Fluids **17**, 065108 (2005).
[31] S. H. Kim and H. Pitsch, Phys. Fluids **18**, 115104 (2007).
[32] N. Chakraborty, Phys. Fluids **19**, 105109 (2007).
[33] N. Chakraborty and N. Swaminathan, Phys. Fluids **19**, 045103 (2007).
[34] N. Chakraborty, M. Klein, and N. Swaminathan, Proc. Combust. Inst. **32**, 1409 (2009).
[35] P. E. Hamlington, A. Y. Poludnenko, and E. S. Oran, Phys. Fluids **23**, 125111 (2011).
[36] L. Cifuentes, C. Dopazo, J. Martin, and C. Jimenez, Phys. Fluids **26**, 065108 (2014).
[37] A. N. Lipatnikov, V. A. Sabelnikov, S. Nishiki, and T. Hasegawa, Phys. Fluids **30**, 081702 (2018).
[38] L. Cifuentes, C. Dopazo, A. Sandeep, N. Chakraborty, and A. M. Kempf, Phys. Fluids **30**, 095101 (2018).
[39] A. N. Lipatnikov, V. A. Sabelnikov, S. Nishiki, and T. Hasegawa, Phys. Fluids **31**, 055101 (2019).
[40] R. Sankaran, E. R. Hawkes, J. H. Chen, T. Lu, and C. K. Law, Proc. Combust. Inst. **31**, 1291 (2007).
[41] R. Yu and X.-S. Bai, Combust. Flame **160**, 1706 (2013).
[42] H. Wang, E. R. Hawkes, J. H. Chen, B. Zhou, Z. Li, and M. Aldén, J. Fluid Mech. **815**, 511 (2017).
[43] S. Chaudhuri, H. Kolla, H. L. Dave, E. R. Hawkes, J. H. Chen, and C. K. Law, Combust. Flame **184**, 273 (2017).
[44] P. A. Libby, J. Fluid Mech. **68**, 273 (1975).
[45] M. Klein, N. Chakraborty, K. W. Jenkins, and R. S. Cant, Phys. Fluids **18**, 055102 (2006).
[46] B. Bobbitt, S. Lapointe, and G. Blanquart, Phys. Fluids **28**, 015101 (2016).
[47] A. J. Aspden, M. J. Day, and J. B. Bell, Combust. Flame **166**, 266 (2016).
[48] C. H. Gibson, Phys. Fluids **11**, 2305 (1968).
[49] A. Soika, F. Dinkelacker, and A. Leipertz, Proc. Combust. Inst. **27**, 785 (1998).
[50] F. Dinkelacker, A. Soika, D. Most, D. Hofmann, A. Leipertz, W. Polifke, and K. Döbbeling, Proc. Combust. Inst. **27**, 857 (1998).
[51] Y.-C. Chen and R. W. Bilger, Combust. Flame **131**, 400 (2002).
[52] L. P. H. de Goey, T. Plessing, R. T. E. Hermanns, and N. Peters, Proc. Combust. Inst. **30**, 859 (2005).
[53] D. A. Knaus, S. S. Sattler, and F. C. Gouldin, Combust. Flame **141**, 253 (2005).
[54] F. T. C. Yuen and O. L. Gülder, Proc. Combust. Inst. **32**, 1747 (2009).
[55] P. Tamadonfar and O. L. Gülder, Combust. Flame **162**, 115 (2015).
[56] R. Fragner, F. Halter, N. Mazellier, C. Chauveau, and I. Gökalp, Proc. Combust. Inst. **35**, 1527 (2015).
[57] L. Ma, Y. Wu, Q. Lei, W. Xu, and C. D. Carter, Combust. Flame **166**, 66 (2016).
[58] B. R. Chowdhury and B. M. Cetegen, Combust. Flame **178**, 311 (2017).
[59] D. Thevenin, Proc. Combust. Inst. **30**, 629 (2005).
[60] A. Y. Poludnenko and E. S. Oran, Combust. Flame **157**, 995 (2010).
[61] A. J. Aspden, M. S. Day, and J. B. Bell, J. Fluid Mech. **680**, 287 (2011).
[62] S. Lapointe, S. Savard, and G. Blanquart, Combust. Flame **162**, 3341 (2015).
[63] A. W. Skiba, T. M. Wabel, C. D. Carter, S. D. Hammack, J. E. Temme, and J. F. Driscoll, Combust. Flame **189**, 407 (2018).
[64] J. F. Driscoll, Prog. Energy Combust. Sci. **34**, 91 (2008).
[65] V. G. Maz'ja, *Sobolev Spaces* (Springer, New York, 1985).
[66] W. Kollmann and J. H. Chen, Proc. Combust. Inst. **25**, 1091 (1994).
[67] L. Vervisch, E. Bidaux, K. N. C. Bray, and W. Kollmann, Phys. Fluids **7**, 2496 (1995).
[68] J. A. Sethian, *Level Set Methods and Fast Marching Methods: Evolving Interfaces in Computational Geometry, Fluid Mechanics, Computer Vision, and Materials Science*, 2nd ed. (Cambridge University Press, Cambridge, 1999).
[69] A. J. Majda and P. E. Souganidis, Nonlinearity **7**, 1 (1994).
[70] P. F. Embid, A. J. Majda, and P. E. Souganidis, Combust. Sci. Technol. **103**, 85 (1994).
[71] P. F. Embid, A. J. Majda, and P. E. Souganidis, Phys. Fluids **7**, 2052 (1995).
[72] G. K. Batchelor, Proc. R. Soc. London A **213**, 349 (1952).
[73] R. Yu, T. Nilsson, X.-S. Bai, and A. N. Lipatnikov, Combust. Flame **207**, 232 (2019).
[74] R. Yu, A. N. Lipatnikov, and X.-S. Bai, Phys. Fluids **26**, 085104 (2014).
[75] R. Yu, X.-S. Bai, and A. N. Lipatnikov, J. Fluid Mech. **772**, 127 (2015).
[76] R. Yu and A. N. Lipatnikov, Phys. Fluids **29**, 065116 (2017).
[77] R. Yu and A. N. Lipatnikov, Phys. Rev. E **95**, 063101 (2017).
[78] T. Elperin, N. Kleeorin, M. Liberman, A. N. Lipatnikov, I. Rogachevskii, and R. Yu, Phys. Rev. E **96**, 053111 (2017).
[79] R. Yu and A. N. Lipatnikov, Flow Turbul. Combust. **102**, 679 (2019).
[80] R. Yu and A. N. Lipatnikov, Comput. Fluids **187**, 69 (2019).
[81] A. N. Lipatnikov and J. Chomiak, Prog. Energy Combust. Sci. **36**, 1 (2010).
[82] V. A. Sabelnikov and A. N. Lipatnikov, Annu. Rev. Fluid Mech. **49**, 91 (2017).
[83] Y. B. Zel'dovich, G. I. Barenblatt, V. B. Librovich, and G. M. Makhviladze, *The Mathematical Theory of Combustion and Explosions* (Consultants Bureau, New York, 1985).
[84] F. A. Williams, *Combustion Theory*, 2nd ed. (Benjamin/Cummings, Menlo Park, California, 1985).
[85] A. G. Lamorgese, D. A. Caughey, and S. B. Pope, Phys. Fluids **17**, 015106 (2005).
[86] R. Yu, J. Yu, and X.-S. Bai, J. Comput. Phys. **231**, 5504 (2012).
[87] G. Strang, SIAM J. Numer. Anal. **5**, 506 (1968).
[88] G. S. Jiang and C. W. Shu, J. Comput. Phys. **126**, 202 (1996).
[89] R. Yu and X.-S. Bai, J. Comput. Phys. **256**, 234 (2014).
[90] A. N. Lipatnikov and J. Chomiak, Prog. Energy Combust. Sci. **28**, 1 (2002).
[91] H. Carlsson, R. Yu, and X.-S. Bai, Int. J. Hydrogen Energy **39**, 20216 (2014).
[92] H. Carlsson, R. Yu, and X.-S. Bai, Proc. Combust. Inst. **35**, 1425 (2015).
[93] T. Nilsson, H. Carlsson, R. Yu, and X.-S. Bai, Fuel **216**, 627 (2018).
[94] W. E. Lorensen and H. E. Cline, InACM Siggraph Computer Graphics **21**, 163 (1987).